Verification and Validation of HiFiLES: a High-Order LES unstructured solver on multi-GPU platforms

Manuel R. López-Morales *, Jonathan Bull†, Jacob Crabill,‡,
Thomas D. Economon‡, David Manosalvas‡,
Joshua Romero‡, Abhishek Sheshadri‡, Jerry E. Watkins II‡, David M. Williams§,
Francisco Palacios¶, and Antony Jameson‖
Department of Aeronautics and Astronautics, Stanford University, Stanford, CA, 94305

The goal of this paper is to present a verification and validation study of HiFiLES: a high-order LES solver developed in the Aerospace Computing Laboratory (ACL) at Stanford University. HiFiLES has been built on top of SD++ (Castonguay et al.) and achieves high-order spatial discretizations with the Energy-Stable Flux Reconstruction (ESFR) scheme on unstructured grids in two and three dimensions. The high parallelizability of this scheme motivates the solver's ability to run in a multi-GPU (Graphical Processing Unit) environment. We intend for this paper to be the main reference for HiFiLES and serve (with the previous SD++ papers) as a reference for researchers that would like to develop or implement high-order numerical schemes based on an Energy-Stable Flux Reconstruction (ESFR) approach.

I. Introduction

Over the last 20 years, much fundamental work has been done in developing high-order numerical methods for Computational Fluid Dynamics. Moreover, the need to improve and simplify these methods has attracted the interest of the applied mathematics and the engineering communities. Now, these methods are beginning to prove themselves sufficiently robust, accurate, and efficient for use in real-world applications.

However, low-order numerical methods are still the standard in the aeronautical industry. There has been a long-term, sustained scientific and economical investment to develop this successful and robust technology. Currently, an industry-standard, second-order finite volume computational tool performs adequately well in a broad range of aeronautical engineering applications. For that reason, the introduction of new, high-order numerical schemes in the aeronautical industry is challenging, particularly in areas where the low-order numerical methods already provide the required robustness and accuracy (keeping in mind the limitations of current turbulence model technology).

Thanks to new and emerging aircraft roles (very small or large concepts, very high or low altitude, quiet vehicles, low fuel consumption vehicles, etc.), revolutionary aircraft design concepts will appear in the near future, and the need for high-fidelity simulation techniques to predict their performance is growing rapidly. Undoubtedly, high-order numerical methods are starting to find their place in the aeronautical industry.

Unsteady simulations, including those of flapping wings, wake capturing, noise prediction, and turbulent flows via Large Eddy Simulation (LES), are just a few examples of computations that could benefit from high-order numerical methods. In particular, high-order methods have a significant edge in applications that require accurate resolution of the smallest scales of the flow. Such situations include the generation and propagation of acoustic noise from an airframe, or at the limits of the flight envelope where unsteady, vortex-dominated flows have a significant effect on aircraft performance. On a given grid, utilizing a high-order representation enables smaller scales to be resolved with a greater degree of accuracy than standard second-order methods. Furthermore, high-order methods are inherently less dissipative, resulting in less unwanted interference with the correct development of the turbulent energy cascade.

*Ph.D. Candidate, Department of Aeronautics and Astronautics, Stanford University, AIAA Student Member; mlopez14@stanford.edu
†Postdoctoral Scholar, Department of Aeronautics and Astronautics, Stanford University, AIAA Member
‡Ph.D. Candidates (authors in alphabetical order), Department of Aeronautics and Astronautics, AIAA Student Members
§Aerodynamics Engineer, CFD & Geometry Group, Flight Sciences, Boeing Commercial Airplanes, AIAA Member
¶Engineering Research Associate, Department of Aeronautics and Astronautics, AIAA Senior Member
‖Thomas V. Jones Professor of Engineering, Department of Aeronautics and Astronautics, Stanford University, AIAA Fellow

This factor makes the combination of high-order numerics with LES modeling very powerful, with the potential to significantly improve upon the accuracy and computational cost of the standard approach of coupling LES with second-order methods. The amount of computing effort to achieve a small error tolerance can also be much smaller with high-order than second-order methods. Even real time simulations (one second of computational time, one second of real flight), could benefit from high-order algorithms that feature more intensive computation within each mesh element (ideal for vector machines and new computational platforms like GPUs, FPGAs, coprocessors, etc).

However, before claiming the future success of high-order numerical methods in industry, two main difficulties should be overcome: a) high-order numerical schemes must be as robust as state-of-the-art low-order numerical methods, b) the existing level of verification and validation (V&V) in high-order CFD codes should be similar to the typical level of their low-order counterparts.

During the last decade, the Aerospace Computing Laboratory (ACL) of the Department of Aeronautics and Astronautics at Stanford University has developed a series of high-order numerical schemes and computational tools that have demonstrated the viability of these schemes. In this paper, a new code named HiFiLES, developed in the ACL and built on top of SD++ (Castonguay et al.[1]), is described in detail with a particular emphasis on robustness in a range of applications and V&V. HiFiLES takes advantage of the synergies between applied mathematics, aerospace engineering, and computer science in order to achieve the ultimate goal of developing an advanced high-fidelity simulation environment.

In addition to the original characteristics of the SD++ code, HiFiLES includes some important physical models and computational methods such as: LES using explicit filters and advanced subgrid-scale (SGS) models, high-order stabilization techniques, shock detection and capturing for compressible flow calculations, convergence acceleration methodologies like p-multigrid, and local and dual time stepping. Some of these techniques will be described in this or related papers.

During the development of this software, several key decisions have been made to guarantee a flexible and lasting infrastructure for industrial Computational Fluid Dynamics simulations:

- The selection of the Energy-Stable Flux Reconstruction (ESFR) scheme on unstructured grids. The flexibility of this method has been critical to guarantee a correct solution independently of the particular physical characteristics of the problem.

- High performance, materialized in a multi-GPU implementation that takes advantage of the ease of parallelization afforded by discontinuous solution representation. Furthermore, HiFiLES aims to guarantee compatibility with future vector machines and revolutionary hardware technologies.

- Code portability by using ANSI C++ and relying on widely-available, and well-supported mathematical libraries like Blas, LAPACK, CuBLAS and ParMetis.

- Object oriented structure to boost the re-usability and encapsulation of the code. This abstraction enables modifications without incorrectly affecting other portions of the code. Although some level of performance is traded for re-usability and encapsulation, the loss in performance is minor.

As the mathematical basis and computational implementation of HiFiLES have been described in previous work[1], the goal of this paper is to illustrate the level of robustness of HiFiLES for interesting problems. This will be accomplished via a verification and validation study, which is fundamental for increasing the credibility of this technology in a competitive industrial framework.

In particular, to ensure that the implementation of the aforementioned features in HiFiLES is correct, the following verification tests are shown: checks of spatial order of accuracy using the Method of Manufactured Solutions (MMS) in 2D and 3D for viscous flows in unstructured grids. After the Verification, a detailed Validation of the code is presented to illustrate that the solutions provided by HiFiLES are an accurate representation of the real world. Simulations of complex flows are validated against experimental or Direct Numerical Simulation (DNS) results for the following cases: laminar flat-plane, flow around a circular cylinder, SD7003 wing-section and airfoil at 4° angle of attack, the Taylor-Green Vortex, and LES of a square cylinder.

The organization of this paper is as follows. Section II. provides a description of the governing equations. Section III. describes the mathematical and numerical algorithms implemented in the code. Section IV. focuses on the V & V of HiFiLES, and finally, the conclusions are summarized in Section V..

Finally, it is our intent for this paper to be the main reference for work that uses or enhances the capabilities of HiFiLES, and for it to serve as a sort of reference for researchers and engineers that would like to develop or implement high-order numerical schemes based on an Energy-Stable Flux Reconstruction (ESFR) approach.

II. Governing Equations

A. Navier Stokes equations

The Navier-Stokes[2] equations provide a complete (dynamical) description of a viscous fluid and express the conservation of mass, momentum, and energy. The complete system of equations (without source terms and assuming adiabatic boundary conditions at the solid wall) can be written in the following conservative form:

$$\frac{\partial U}{\partial t} + \nabla \cdot \mathbf{F} = 0 \tag{1}$$

where $\mathbf{F} = (F, G, H) = (F_I, G_I, H_I) - (F_V, G_V, H_V)$ and

$$U = \begin{pmatrix} \rho \\ \rho u \\ \rho v \\ \rho w \\ \rho e \end{pmatrix} \quad F_I = \begin{pmatrix} \rho u \\ \rho u^2 + p \\ \rho uv \\ \rho uw \\ \rho ue + pu \end{pmatrix} \quad G_I = \begin{pmatrix} \rho v \\ \rho vu \\ \rho v^2 + p \\ \rho vw \\ \rho ve + pv \end{pmatrix} \quad H_I = \begin{pmatrix} \rho w \\ \rho wu \\ \rho wv \\ \rho w^2 + p \\ \rho we + pw \end{pmatrix} \tag{2}$$

$$F_V = \begin{pmatrix} 0 \\ \sigma_{xx} \\ \sigma_{xy} \\ \sigma_{xz} \\ u_i\sigma_{ix} - q_x \end{pmatrix} \quad G_V = \begin{pmatrix} 0 \\ \sigma_{yx} \\ \sigma_{yy} \\ \sigma_{yz} \\ u_i\sigma_{iy} - q_y \end{pmatrix} \quad H_V = \begin{pmatrix} 0 \\ \sigma_{zx} \\ \sigma_{zy} \\ \sigma_{zz} \\ u_i\sigma_{iz} - q_z \end{pmatrix} \tag{3}$$

As usual, ρ is density, u, v, w are the velocity components in the x, y, z directions, respectively, and e is total energy per unit mass. In HiFiLES, the pressure is determined from the ideal gas equation of state

$$p = (\gamma - 1)\rho \left(e - \frac{1}{2}\left(u^2 + v^2 + w^2\right) \right) \tag{4}$$

the viscous stresses are those of a Newtonian fluid

$$\sigma_{ij} = \mu \left(\frac{\partial u_i}{\partial x_j} + \frac{\partial u_j}{\partial x_i} \right) - \frac{2}{3}\mu\delta_{ij}\frac{\partial u_k}{\partial x_k} \tag{5}$$

and the heat fluxes are defined as

$$q_i = -k\frac{\partial T}{\partial x_i} \tag{6}$$

where

$$k = \frac{C_p\mu}{\mathrm{Pr}}, \quad T = \frac{p}{R\rho} \tag{7}$$

Pr is the Prandtl number, C_p is the specific heat at constant pressure and R is the gas constant. In the case of air, $\gamma = 1.4$ and $\mathrm{Pr} = 0.72$. The dynamic viscosity μ in HiFiLES can be a constant or a function of temperature using Sutherland's law.

B. Reynolds Averaged Navier-Stokes (RANS) equations

The compressible Navier-Stokes equations can be used to solve a variety of different flow physics problems, but for turbulent flows, direct numerical simulation using these equations can become excessively expensive. For engineering applications, it is customary to perform a Favre averaging procedure on the Navier-Stokes equations in order to solve for turbulent mean quantities. This leads to a variety of terms which must be modeled in order to provide closure to the resulting RANS equations[3,4]. For example, using the one equation Spalart-Allmaras (SA) turbulence model, the conservative form of the RANS equations is very similar to the Navier-Stokes equations with the following extra terms included in Eq. 2:

$$U_{\tilde{\nu}} = \rho\tilde{\nu}, \quad F_{I,\tilde{\nu}} = \rho u\tilde{\nu}, \quad G_{I,\tilde{\nu}} = \rho v\tilde{\nu}, \quad H_{I,\tilde{\nu}} = \rho w\tilde{\nu}, \tag{8}$$

$$F_{V,\tilde{\nu}} = \frac{1}{\sigma}(\mu + \mu\psi)\frac{\partial\tilde{\nu}}{\partial x}, \quad G_{V,\tilde{\nu}} = \frac{1}{\sigma}(\mu + \mu\psi)\frac{\partial\tilde{\nu}}{\partial y}, \quad H_{V,\tilde{\nu}} = \frac{1}{\sigma}(\mu + \mu\psi)\frac{\partial\tilde{\nu}}{\partial w}, \tag{9}$$

$$S_{\tilde{\nu}} = c_{b_1}\tilde{S}\rho\nu\psi + \frac{1}{\sigma}\left[c_{b_2}\rho\nabla\tilde{\nu}\cdot\nabla\tilde{\nu}\right] - c_{w_1}\rho f_w\left(\frac{\nu\psi}{d}\right)^2. \tag{10}$$

Note that the flow variables have been redefined as Favre-averaged quantities and $S_{\tilde{\nu}}$ is a source term that would appear on the right hand side of Equation (1). Also, the viscous stresses (Eq. 5) now include the Boussinesq approximated Reynolds stress terms,

$$\sigma_{ij} = (\mu+\mu_t)\left(\frac{\partial u_i}{\partial x_j}+\frac{\partial u_j}{\partial x_i}\right) - \frac{2}{3}(\mu+\mu_t)\delta_{ij}\frac{\partial u_k}{\partial x_k} \tag{11}$$

and the heat fluxes are redefined as

$$q_i = -C_p\left(\frac{\mu}{\mathrm{Pr}}+\frac{\mu_t}{\mathrm{Pr}_t}\right)\frac{\partial T}{\partial x_i} \tag{12}$$

where μ_t is the dynamic eddy viscosity and Pr_t is the turbulent Prandtl number. The various terms added by the one equation SA turbulence model are more precisely defined in Section D..

III. Numerical Methods

In this section the main numerical techniques implemented in HiFiLES will be described. We will emphasize the critical role of the selected numerical discretization (Flux Reconstruction Method), and its capability to solve CFD problems using unstructured meshes.

A. Flux Reconstruction Method

What follows is an overview of the flux reconstruction (FR) framework. We start the discussion with the solution of the advection-diffusion equation in one dimension using the FR approach to illustrate the method. We then proceed to briefly explain how conservation equations can be solved in multiple dimensions. The Navier-Stokes equations are a set of coupled conservation equations in multiple dimensions, so the extension of the FR methodology to them is straightforward. The detailed description of the algorithm used in HiFiLES is given by Castonguay et al.[1].

1. Solution of the Advection Equation in One Dimension using the FR Approach

Consider the one-dimensional conservation law

$$\frac{\partial u}{\partial t}+\frac{\partial f}{\partial x} = 0 \tag{13}$$

in domain Ω, where x is the spatial coordinate, t is time, u –the *solution*– is a scalar function of x and t, and f –the *flux*– is a scalar function of u. Note that by letting $f = f(u, \frac{\partial u}{\partial x})$, Equation 13 becomes a model of the Navier-Stokes equations.

Let us partition the domain $\Omega = [x_1, x_{N+1})$ into N non-overlapping elements with interfaces at $x_1 < x_2 < ... < x_{N+1}$. Then,

$$\Omega = \bigcup_{n=1}^{N}\Omega_n \tag{14}$$

and $\Omega_n = [x_n, x_{n+1})$ for $n = 1, ..., N$. To simplify the implementation, let us map each of the physical elements Ω_n to a standard element $\Omega_s = [-1, 1)$ with the function $\Theta_n(\xi)$, where

$$x = \Theta_n(\xi) = \left(\frac{1-\xi}{2}\right)x_n + \left(\frac{1+\xi}{2}\right)x_{n+1} \tag{15}$$

With this mapping, the evolution of u within each Ω_n can be determined with the following transformed conservation equation

$$\frac{\partial \hat{u}}{\partial t}+\frac{1}{J_n}\frac{\partial \hat{f}}{\partial \xi} = 0 \tag{16}$$

where

$$\hat{u} = u(\Theta_n(\xi), t) \text{ in } \Omega_n \tag{17}$$

$$\hat{f} = f(\Theta_n(\xi), t) \text{ in } \Omega_n \tag{18}$$

$$J_n = \left.\frac{\partial x}{\partial \xi}\right|_{\Omega_n} \tag{19}$$

Now, we introduce polynomials of degree p, $\hat{u}^\delta$ and $\hat{f}^\delta$, to approximate the exact values $\hat{u}$ and $\hat{f}$, respectively. We can write these polynomials as

$$\hat{u}^\delta = \sum_{i=1}^{N_s} \hat{u}_i^\delta l_i(\xi) \tag{20}$$

$$\hat{f}^\delta = \sum_{i=1}^{N_s} \hat{f}_i^\delta l_i(\xi) \tag{21}$$

where N_s is the number of solution points, $\hat{u}_i^\delta$ is the current value of the solution approximation function at the i^{th} *solution point* in the reference element, $\hat{f}_i^\delta$ is the current value of the flux approximation function at the i^{th} *flux point* in the reference element, l_i is the Lagrange polynomial equal to 1 at the i^{th} solution point and 0 at the others, and δ denotes that the function is an approximation.

Note that the piecewise polynomials might not be continuous (or C^0) across the interfaces. In the Flux Reconstruction approach, the flux used in the time advancement of the solution is made C^0 by introducing flux correction functions.

This can be achieved by finding interface solution values at each element boundary and then correcting the solution. Let $\hat{u}_L^{\delta I}$ and $\hat{u}_R^{\delta I}$ be the interface solution values at left and right boundaries of some element, respectively. $\hat{u}_L^{\delta I}$ and $\hat{u}_R^{\delta I}$ can be found with a Riemann solver for Discontinuous-Galerkin (DG) methods[5]. Then, select solution correction functions g_L and g_R such that

$$g_L(-1) = 1 \ , \ g_L(1) = 0 \tag{22}$$

$$g_R(-1) = 0 \ , \ g_R(1) = 1 \tag{23}$$

and let

$$\hat{u}^C = \hat{u}^\delta + (\hat{u}_L^{\delta I} - \hat{u}_L^\delta) g_L + (\hat{u}_R^{\delta I} - \hat{u}_R^\delta) g_R \tag{24}$$

where superscript C denotes the function has been made continuous (or has been corrected), and $\hat{u}_L^\delta$, $\hat{u}_R^\delta$ represent the solution approximation evaluated at the left and right boundaries.

Using the values of $\hat{u}_i^\delta$ and $\frac{\partial \hat{u}^C}{\partial \xi}|_{\xi_i}$ we then find

$$\hat{f}_i^\delta = \hat{f}\left(\hat{u}_i^\delta, \frac{1}{J_n}\left.\frac{\partial \hat{u}^C}{\partial \xi}\right|_{\xi_i}\right) \text{ in element } \Omega_n$$

We can proceed in a similar fashion to correct the flux to obtain

$$\hat{f}^C = \hat{f}^\delta + (\hat{f}_L^{\delta I} - \hat{f}_L^\delta) h_L + (\hat{f}_R^{\delta I} - \hat{f}_R^\delta) h_R \tag{25}$$

where h_R and h_L are right and left flux correction functions satisfying the same boundary conditions as g_R and g_L, respectively, and $\hat{f}_L^{\delta I}$ and $\hat{f}_R^{\delta I}$ are the interface fluxes found via a Riemann solver. Note that if the flux corresponds to linear advection, correcting the solution and correcting the flux are equivalent steps.

The solution can then be advanced at each solution point. In semi-discrete form, this is

$$\frac{d\hat{u}_i^\delta}{dt} = -\frac{\partial \hat{f}^C}{\partial \xi}(\xi_i) \tag{26}$$

The FR scheme can be made provably stable for the linear advection-diffusion equation by selecting special types of correction functions[6]. In general, these correction functions are polynomials of degree $p+1$ so both sides in Equation (26) are quantities related to polynomials of order p –for consistency[7].

Vincent et al.[8] have shown that in the case of the 1-dimensional, linear advection equation, the Flux Reconstruction approach can be proven to be stable for a specific family of correction functions parameterized by a scalar called c. In addition, they showed that by selecting specific values of c it is possible to recover a particular nodal Discontinuous Galerkin (DG) method and Spectral Difference (SD), plus a FR scheme that was previously found to be stable by Huynh[9].

B. Extension to Multiple Dimensions

Extension to multiple dimensions requires formulating multi-dimensional interpolation functions and correction functions that satisfy boundary conditions equivalent to those in Equation (22) for each type of element.

Interpolation bases for quadrilaterals and hexahedra can be obtained via tensor products of the 1-dimensional interpolation basis. In HiFiLES, we discretize the solution in 3-dimensions in the following way

$$\hat{\mathbf{u}}^{\delta}(\xi,\eta,\zeta) = \sum_{i=1}^{p+1}\sum_{j=1}^{p+1}\sum_{k=1}^{p+1} \hat{\mathbf{u}}^{\delta}_{i,j,k} l_i(\xi) l_j(\eta) l_k(\zeta) \tag{27}$$

where i, j, k index the solution points along the ξ, η, ζ directions, respectively. The flux is discretized similarly.

The interpolation basis for triangles are described in detail by Castonguay et al.[10] and Williams et al.[11]. The formulation for tetrahedra is detailed by Williams et al.[12]. The extension of interpolation polynomials to prisms is obtained via tensor products of the 1-dimensional basis with the triangular basis[1].

In general, the boundary conditions for the correction functions in multiple dimensions can be formulated as

$$\mathbf{h}_i(\vec{\xi_j}) \cdot \mathbf{n}_j = \delta_{ij} \tag{28}$$

where $\mathbf{h}_i$ is the vector of correction functions associated with interface point i, $\vec{\xi_j}$ is the location vector of the j^{th} interface point, $\mathbf{n}_j$ is the outward unit normal at interface point j, and δ_{ij} is the Kronecker delta. Interface points are located on the boundary of an element.

One of the challenges in the FR approach is finding correction functions that not only satisfy Equation (28) but also guarantee stability in the linear advection-diffusion case. Correction functions that guarantee such stability exist for 1-dimensional segments[8], triangles[10,11], and tetrahedra[12]. FR schemes with these correction functions comprise the ESFR family of schemes.

Although formal proofs of stability for the linear advection equation do not exist yet for quadrilaterals, hexahedra, and prisms, it has been observed that the tensor products of provably stable correction functions used in these elements maintain stability. In addition, as of now HiFiLES does not have an implementation for pyramidal elements, mostly because of the challenges involved in finding the respective correction functions that guarantee stability. Nevertheless, a suggested approach to find such correction functions has been presented by Jameson[13].

With regards to time integration, HiFiLES uses an explicit Adaptive Runge-Kutta 45 (RK45) Method and local or global time stepping. In addition, a polynomial multigrid to improve code convergence is currently being validated.

C. Shock Capturing and Stabilization Models

We use the method of concentration described in[14] for detecting shocks on meshes with quadrilateral elements. We are still in the process of extending the method of concentration to triangles and are currently using Persson and Peraire's method[15,16] for the same. We have explored both selective addition of artificial viscosity as well as modal order reduction for capturing the detected shocks effectively. Persson and Peraire have used this shock capturing tool as a stabilization method as well in their turbulence calculations. Here we show a viscous case on quads using concentration method (reproduction of the result in[14]) and an inviscid case on triangles using Persson and Peraire's method.

Figures 1 and 2 show the density and energy plots for a Mach 1.2 flow over a NACA 0012 airfoil at a 5° angle of attack. The flow is at Reynolds number of 60000 and we have used 6th order polynomial interpolation in the elements for the computation. There is a bow shock in front of the airfoil and we see fish-tail shocks at the trailing edge. We can also see boundary layer formation and a Λ-shock structure on the upper side of the airfoil. Here we have used simple modal order reduction in elements with the shock sensor value above a certain threshold. Figure 3 shows the elemental shock sensor values. We can see the shock sensor is able to distinguish between shocks and other smooth regions enabling the structure of the vortices and boundary layer to be preserved.

Figure 4 shows an inviscid flow of M = 1.6 over a Naca 0012 airfoil at 0° angle of attack on a triangle mesh. Here we use Persson and Peraire's method for shock detection, and we can see that the shock has been detected and captured well. A few oscillations still remain near the strong bow shock in front of the airfoil even after enforcement of continuity of the artificial viscosity coefficients. Figures 5 and 6 show the artificial viscosity being added element-wise and after continuity enforcement respectively.

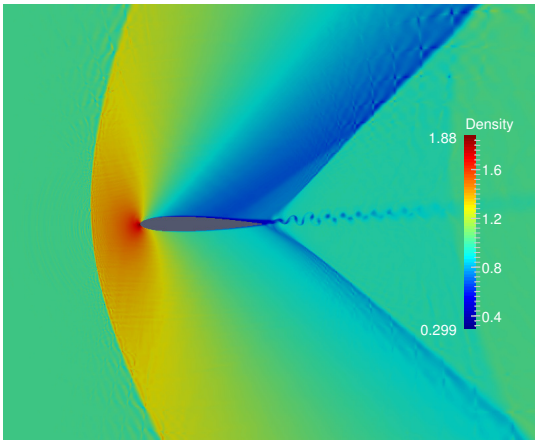

Figure 1: Density contours for viscous flow at M = 1.2 over a NACA 0012 airfoil at 5° AoA with polynomial order 6

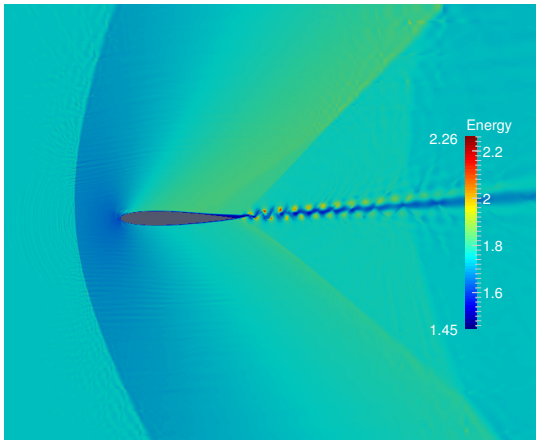

Figure 2: Energy contours

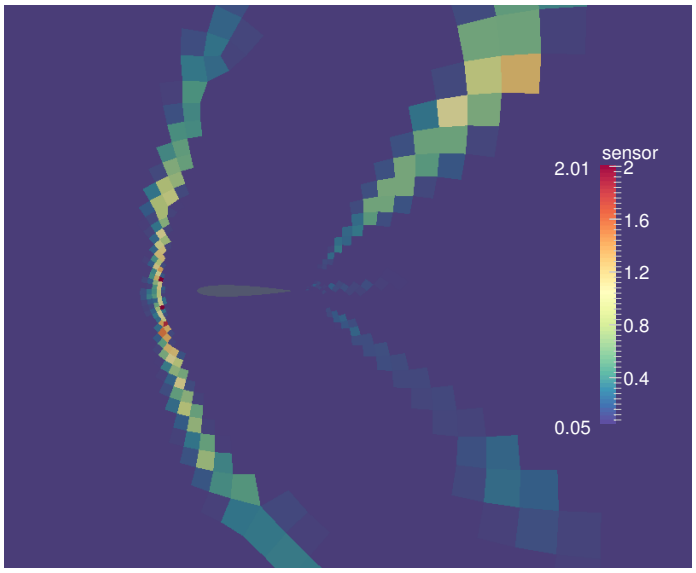

Figure 3: This figure shows the elemental shock "sensor" for the M = 1.2 viscous case shown in Figure 1

D. Spalart-Allmaras (SA) Turbulence Model and Negative $\tilde{\nu}$ Modification

The one equation SA turbulence model is one of the more commonly used turbulence models for solving attached and moderately separated aerodynamic flows[17]. The added equation directly solves for turbulent eddy viscosity via advection, diffusion, production and dissipation. A modified form of the equation can be written as[4,18,19]:

$$\frac{\partial}{\partial t}(\rho\tilde{\nu}) + \nabla\cdot(\rho\tilde{\nu}\boldsymbol{u}) = c_{b_1}\tilde{S}\rho\nu\psi + \frac{1}{\sigma}\left[\nabla\cdot((\mu+\mu\psi)\nabla\tilde{\nu}) + c_{b_2}\rho\nabla\tilde{\nu}\cdot\nabla\tilde{\nu}\right] - c_{w_1}\rho f_w\left(\frac{\nu\psi}{d}\right)^2 \tag{29}$$

where $\tilde{\nu}$ is a modified version of the kinematic eddy viscosity and ν is the kinematic viscosity. The other variables are defined as:

$$\mu_t = \begin{cases} \rho\tilde{\nu}f_{v_1} & \text{if } \tilde{\nu}\geq 0 \\ 0 & \text{if } \tilde{\nu}<0 \end{cases} \quad \text{where} \quad f_{v_1} = \frac{\left(\frac{\rho\tilde{\nu}}{\mu}\right)^3}{\left(\frac{\rho\tilde{\nu}}{\mu}\right)^3 + c_{v_1}^3} \tag{30}$$

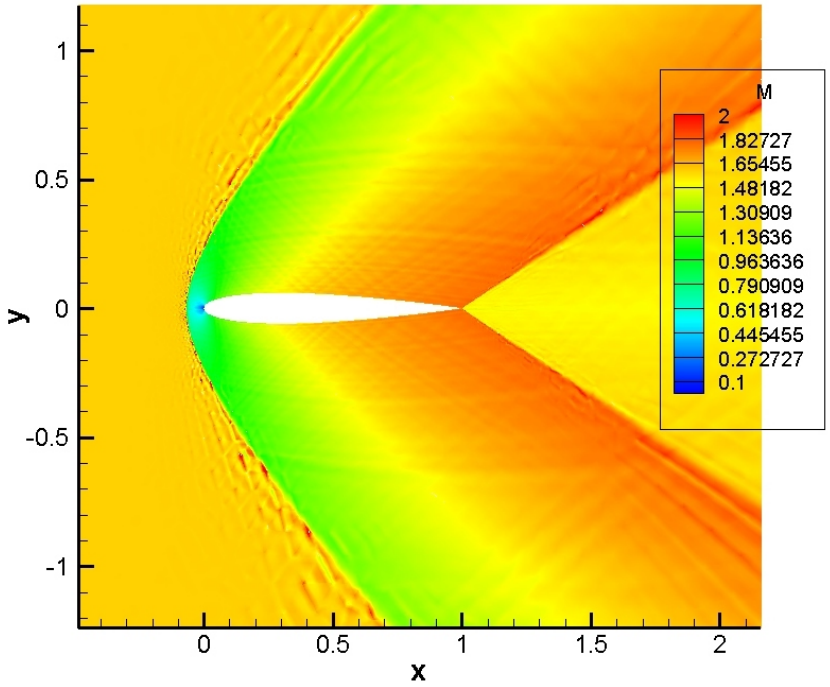

Figure 4: Mach contours for inviscid flow over NACA 0012 at M = 1.6 and AoA = 0° on a triangle-mesh using Persson and Peraire's method

$$\tilde{S} = \begin{cases} S + \bar{S} & \text{if } \bar{S} \geq -c_{v_2} S \\ S + \frac{S(c_{v_2}^2 S + c_{v_3} \bar{S})}{(c_{v_3} - 2c_{v_2})S - \bar{S}} & \text{if } \bar{S} \leq -c_{v_2} S \end{cases} \tag{31}$$

$$S = \sqrt{\boldsymbol{\omega} \cdot \boldsymbol{\omega}} \qquad \bar{S} = \frac{(\nu\psi)^2 f_{v_2}}{\kappa^2 d^2} \tag{32}$$

$$f_{v_2} = 1 - \frac{\psi}{1 + \psi f_{v_1}} \tag{33}$$

$$f_w = g\left[\frac{1 + c_{w_3}^6}{g^6 + c_{w_3}^6}\right]^{1/6} \qquad g = r + c_{w_2}(r^6 - r) \qquad r = \frac{\nu\psi}{\tilde{S}\kappa^2 d^2} \tag{34}$$

where S is the magnitude of vorticity, d is the distance to the closest wall, $c_{b1} = 0.1355$, $\sigma = \frac{2}{3}$, $c_{b2} = 0.622$, $K = 0.41$, $\text{Pr}_t = 0.9$, $c_{v1} = 7.1$, $c_{v2} = 0.7$, $c_{v3} = 0.9$, $c_{w1} = \frac{c_{b1}}{K^2} + \frac{(1+c_{b2})}{\sigma}$, $c_{w2} = 0.3$, and $c_{w3} = 2$.

The diffusion term, $\nabla \cdot (\rho\tilde{\nu}\boldsymbol{u})$, may become discontinuous in the first derivative leading to oscillations in high-order polynomials. This can lead to large negative values of the modified eddy viscosity term, $\tilde{\nu}$, significant enough to cause an unbounded solution. To prevent this, the following modification is introduced[19].

$$\psi = \begin{cases} 0.05log(1.0 + e^{(20.0\chi)}) & \text{if } \chi \leq 10.0, \\ \chi & \text{if } \chi > 10.0, \end{cases} \tag{35}$$

$$\chi = \frac{\tilde{\nu}}{\nu} \tag{36}$$

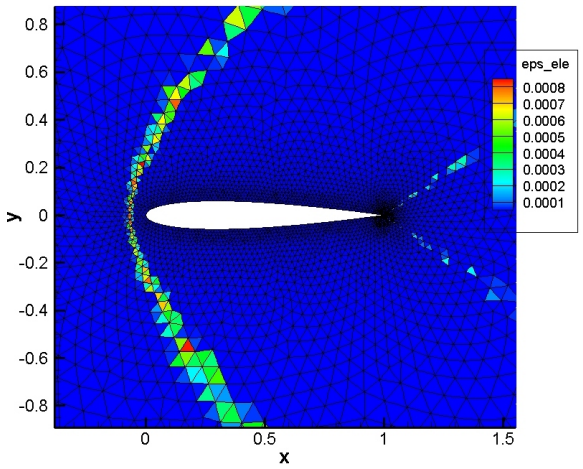

Figure 5: Element-wise AV coefficients for the inviscid M 1.6 case

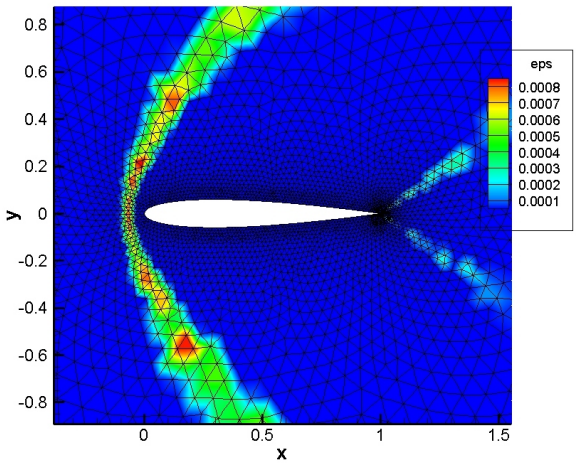

Figure 6: AV coefficients with continuity enforcement

E. Large Eddy Simulation

In order to resolve all the scales of motion in a high Reynolds number turbulent flow, the computational mesh would have to be exceedingly fine. A practical solution is to employ the Large Eddy Simulation (LES) formulation, which only resolves the larger scales of motion and thus allows for the use of coarser meshes.

The effect of the unresolved or subgrid-scale (SGS) dynamics on the solution is accounted for by an SGS model for the subgrid-scale stress τ_{ij}, which is added to the viscous stress tensor σ_{ij} given by (5):

$$\sigma_{ij} = 2\mu S^d_{ij} + \tau_{ij}, \tag{37}$$

$$S^d_{ij} = \frac{1}{2}\left(\frac{\partial u_i}{\partial x_j} + \frac{\partial u_j}{\partial x_i} - \frac{2}{3}\delta_{ij}\frac{\partial u_k}{\partial x_k}\right). \tag{38}$$

The standard Smagorinsky model[20] is available in HiFiLES:

$$\tau_{ij} = 2\mu_t S^d_{ij}, \tag{39}$$

$$\mu_t = \rho C_S^2 \triangle^2 |S^d|, \tag{40}$$

$$|S^d| = \sqrt{2 S^d_{ij} S^d_{ij}}, \tag{41}$$

where μ_t is the eddy viscosity, $C_S = 0.1$ is the Smagorinsky coefficient and $\triangle$ is the filter width. In HiFiLES the filter width is given by (in 3D):

$$\triangle = \alpha(\text{vol})^{1/3}, \tag{42}$$

where $\alpha \geq 1$ is a user-defined scaling factor and vol is the element volume.

HiFiLES also includes the Wall-Adapting Local Eddy-Viscosity (WALE) model[21] and the Similarity model[22]. The Similarity model incorporates a low-pass filtering operator, for which several choices are available in HiFiLES: a discrete Gaussian filter[23], a high-order commuting Vasilyev-type filter[24,25] and a modal Vandermonde-type filter[26].

The modal filter can be used on unstructured tetrahedral meshes. For details of these operators, see Lodato, Castonguay and Jameson[23] and Bull and Jameson[27]. One can combine the similarity model with the Smagorinsky or WALE model to form a mixed SGS model. The WALE-similarity mixed (WSM) model, first proposed by Lodato et al.[28], was used in simulations of the flow over a square cylinder (see Section G.).

F. Computing Architecture and Scalability

The HiFiLES code has been designed to work on multi-CPU as well as multi-CPU-GPU platforms. The Flux Reconstruction method in its current form with explicit time-stepping has a great potential for parallelization. Since the

solution points are not explicitly shared between elements, most of the computations are element-local enabling an efficient use of shared memory on GPUs. Also, several computations are independent for each solution point and the highly parallelizable nature of GPUs becomes very useful. A detailed description of the parallelization of the FR method, along with scalability and performance analysis has been performed in [1].

IV. Verification and Validation

A. Method of Manufactured Solutions

This section describes the test of HiFiLES's spatial order of accuracy using the Method of Manufactured Solutions (MMS) in 2D and 3D for viscous flows. As shown by Salari et. al[29], the MMS test rigorously assesses the correctness of implementation of a solver of Partial Differential Equations. We perform the MMS test in grids using simplex elements, as these are crucial for simulations in unstructured meshes and have a more complex implementation than squares and hexahedra.

The MMS test for NS solvers requires checking the solver's solution against an exact solution. Such an exact solution can be chosen arbitrarily. The NS equations can be satisfied with this arbitrary solution by including a time-dependent source term in the equations. Then, we solve

$$\frac{\partial U}{\partial t} + \nabla \cdot \mathbf{F} = S \tag{43}$$

For the following tests, we selected a smooth exact solution, so aliasing does not pollute the results. We picked

$$U_{2D} = \begin{pmatrix} \sin\left(k(x+y) - \omega t\right) + a \\ \sin\left(k(x+y) - \omega t\right) + a \\ \sin\left(k(x+y) - \omega t\right) + a \\ \left(\sin\left(k(x+y) - \omega t\right) + a\right)^2 \end{pmatrix} \quad U_{3D} = \begin{pmatrix} \sin\left(k(x+y+z) - \omega t\right) + a \\ \sin\left(k(x+y+z) - \omega t\right) + a \\ \sin\left(k(x+y+z) - \omega t\right) + a \\ \sin\left(k(x+y+z) - \omega t\right) + a \\ \left(\sin\left(k(x+y+z) - \omega t\right) + a\right)^2 \end{pmatrix} \tag{44}$$

To find the value of S, we plug the values of our selected U into the left-hand side of Equation (44) and simplify. The resulting expression is S. We let Pr$= 0.72, \gamma = 1.4, k = \pi, \omega = \pi, a = 3.0$ and $\mu = 0.001$.

The meshes used have dimensions $[-1, 1] \times [-1, 1]$ in 2D and $[-1, 1] \times [-1, 1] \times [-1, 1]$ in 3D. Periodic boundary conditions were applied on the boundaries of the square and cube domains. Uniform square and cubic meshes were created and then each element was subdivided into triangles or tetrahedra. Two triangles were created from each square, and six tetrahedra were created from each cube. Consequently, in 2D a $N \times N$ mesh contains $2N^2$ triangles, and in 3D a $N \times N \times N$ mesh contains $6N^3$ tetrahedra.

In 3D, the time step was $1\text{e}{-4}$ seconds and 10 seconds of flow were simulated. In 2D, the time step was $1\text{e}{-6}$ seconds and 1 second of flow was simulated. The time-stepping scheme used was the low-storage, 4^{th} order accurate RK45 method[30].

Polynomial Order	Mesh:	2x2x2	4x4x4	8x8x8	16x16x16	Overall Order of Accuracy
$p = 1$	L_2 error	5.76e-01	1.35e-01	3.22e-02	7.90e-03	
	$\mathcal{O}(L_2)$		2.10	2.06	2.03	2.06
$p = 2$	L_2 error	4.09e-01	5.52e-02	6.87e-03	8.53e-04	
	$\mathcal{O}(L_2)$		2.89	3.01	3.01	2.97
$p = 3$	L_2 error	9.77e-02	5.97e-03	3.78e-04		
	$\mathcal{O}(L_2)$		4.03	3.98		4.01
$p = 4$	L_2 error	1.12e-02	6.39e-04	2.07e-05		
	$\mathcal{O}(L_2)$		4.13	4.95		4.54
$p = 5$	L_2 error	1.53e-01	5.08e-03	6.92e-05		
	$\mathcal{O}(L_2)$		4.91	6.20		5.55

Table 1: Accuracy of HiFiLES for NS equations with source term in tetrahedral meshes at $t = 10$. L_2 error is the L_2-norm of the error in the energy field: ρe

Tables (3) and (1) show the spatial order of accuracy achieved when calculating the energy fields ρe in 2D and 3D, respectively. Tables (4) and (2) show the order of accuracy for the gradient of the energy field $\frac{\partial}{\partial x_i}(\rho e)$ in 2D and

Polynomial Order	Mesh:	2x2x2	4x4x4	8x8x8	16x16x16	Overall Order of Accuracy
$p=1$	L_2 error	1.98e+01	9.57e+00	4.55e+00	2.19e+00	
	$\mathcal{O}(L_2)$		1.05	1.07	1.06	1.06
$p=2$	L_2 error	1.17e+01	2.98e+00	7.10e-01	1.71e-01	
	$\mathcal{O}(L_2)$		1.97	2.07	2.06	2.03
$p=3$	L_2 error	3.17e+00	3.81e-01	4.73e-02		
	$\mathcal{O}(L_2)$		3.06	3.01		3.03
$p=4$	L_2 error	5.21e-01	4.27e-02	2.69e-03		
	$\mathcal{O}(L_2)$		3.61	3.99		3.80
$p=5$	L_2 error	3.20e+00	1.88e-01	4.79e-03		
	$\mathcal{O}(L_2)$		4.09	5.29		4.69

Table 2: Accuracy of HiFiLES for NS equations with source term in tetrahedral meshes at $t = 10$. L_2 error is the L_2-norm of the error in the gradient of the energy field: $\frac{\partial}{\partial x_i}(\rho e)$

Polynomial Order	Mesh:	4x4	8x8	16x16	32x32	64x64	Overall Order of Accuracy
$p=1$	L_2 error	7.92e-01	1.84e-01	4.36e-02	1.07e-02	2.68e-03	
	$\mathcal{O}(L_2)$		2.10	2.08	2.03	2.00	2.05
$p=2$	L_2 error	1.29e-01	1.61e-02	1.95e-03	2.33e-04	2.86e-05	
	$\mathcal{O}(L_2)$		3.00	3.05	3.06	3.03	3.04
$p=3$	L_2 error	1.01e-02	9.25e-04	5.71e-05	3.65e-06	2.35e-07	
	$\mathcal{O}(L_2)$		3.45	4.02	3.97	3.96	3.88
$p=4$	L_2 error	2.60e-03	6.33e-05	2.00e-06	6.49e-08	3.62e-09	
	$\mathcal{O}(L_2)$		5.36	4.98	4.95	4.16	4.88
$p=5$	L_2 error	7.15e-05	3.87e-06	6.31e-08			
	$\mathcal{O}(L_2)$		4.21	5.94			5.07

Table 3: Accuracy of HiFiLES for NS equations with source term in triangular meshes at $t = 1$. L_2 error is the L_2-norm of the error in the energy field: ρe

Polynomial Order	Mesh:	4x4	8x8	16x16	32x32	64x64	Overall Order of Accuracy
$p=1$	L_2 error	1.61e+01	8.31e+00	3.81e+00	1.71e+00	7.84e-01	
	$\mathcal{O}(L_2)$		0.96	1.12	1.15	1.13	1.10
$p=2$	L_2 error	4.05e+00	8.16e-01	1.90e-01	4.54e-02	1.11e-02	
	$\mathcal{O}(L_2)$		2.31	2.11	2.06	2.04	2.12
$p=3$	L_2 error	4.71e-01	6.39e-02	7.03e-03	7.75e-04	8.84e-05	
	$\mathcal{O}(L_2)$		2.88	3.18	3.18	3.13	3.11
$p=4$	L_2 error	1.01e-01	4.30e-03	2.31e-04	1.41e-05		
	$\mathcal{O}(L_2)$		4.56	4.22	4.04		4.27
$p=5$	L_2 error	5.04e-03	2.50e-04	7.80e-06			
	$\mathcal{O}(L_2)$		4.33	5.00			4.67

Table 4: Accuracy of HiFiLES for NS equations with source term in triangular meshes at $t = 1$. L_2 error is the L_2-norm of the error in the gradient of the energy field: $\frac{\partial}{\partial x_i}(\rho e)$

3D, respectively. Because of the exact solutions that were picked, the exact values of the gradients of ρe in the x, y, z directions are equal. The "Overall Order of Accuracy" is the slope of the linear best-fit of each of the error vs. grid size data sets.

As expected[5], the order of accuracy of the solution is $p+1$ and the order of accuracy of the gradient of the solution is p, where p is the order of the polynomial used to approximate the solution fields. In the simulations with $p = 5$, the relatively large time step introduces errors larger than the spatial discretization errors. Hence we observe sub-optimal orders of convergence on the coarsest meshes.

B. Subsonic laminar flat-plate

Computations of the flow over a subsonic flat-plate have been performed and validated against the Blasius solution for a laminar boundary layer. The flow conditions are Mach number 0.5, 0° angle of attack and Reynolds number $1 \cdot 10^6$ based on the plate length. The governing equations are the 2D Navier-Stokes equations with constant ratio of specific heats of 1.4, Prandtl number of 0.72 and constant dynamic viscosity of $1.827 \cdot 10^{-5} Pa \cdot s$.

Mesh	First cell height	# of cells in boundary layer	p_3	p_4	p_5	p_6
Mesh a0 (140 = 14x10)	0.00075	2	×	×	×	✓
Mesh a1 (560 = 28x20)	0.000375	4	×	×	✓	✓
Mesh a2 (2240 = 56x40)	0.0001875	8	×	✓	✓	✓
Mesh a3 (8960 = 112x80)	0.0000935	16	✓	✓	✓	✓

Table 5: HiFiLES convergence using different grids and polynomial order. × / ✓ indicates not converged/converged respectively

The objective of this study is to determine the minimum number of elements and the order of polynomial required to converge the flat-plate simulation using HiFILES. Four different numerical grids have been used in this study (with 2, 4, 8, and 16 elements inside the boundary layer) and four polynomial orders (p_3–p_6). The results, summarized in Table 5, show that a minimum number of elements is needed in the boundary layer, depending on the polynomial order, to obtain satisfactory convergence (free from inter-element jumps).

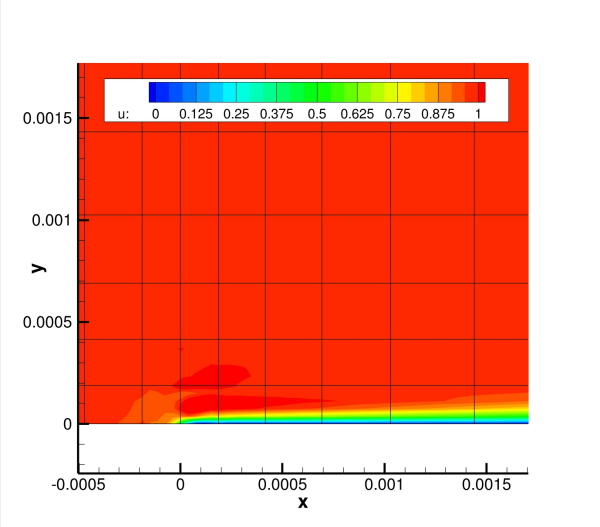

Figure 7: Detail of the flat-plate leading edge (x=0.0, mesh a2). Simulation with $p = 4$.

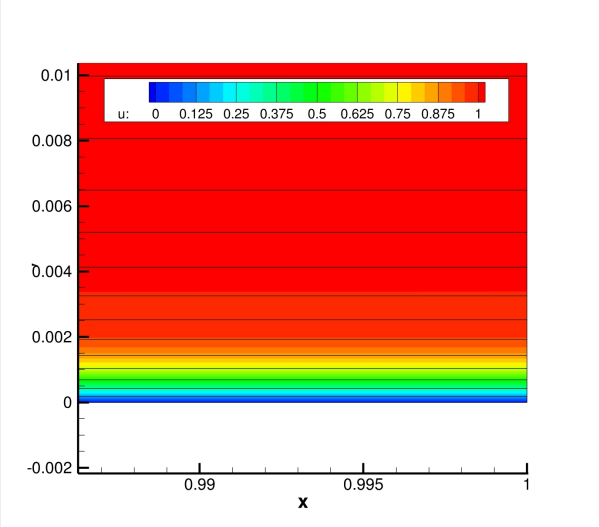

Figure 8: Flow solution at the end of the flat-plate (x=1.0, mesh a2). Simulation with $p = 4$.

The results are compared with the Blasius solution for laminar boundary layer with satisfactory results, and some details of the solutions are presented in Fig. 7 (leading edge), and Fig. 8 (end of the flat-plate). It is important to note that in this particular case (mesh a2) the flat-plate boundary layer is captured using 8 elements, while in a second order solver it would be necessary to place about 30 elements inside the boundary layer.

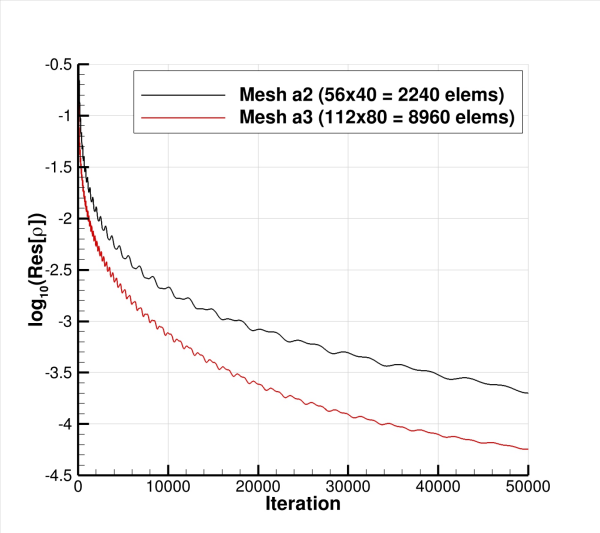

Figure 9: Convergence comparison (3^{rd} order, finest grids).

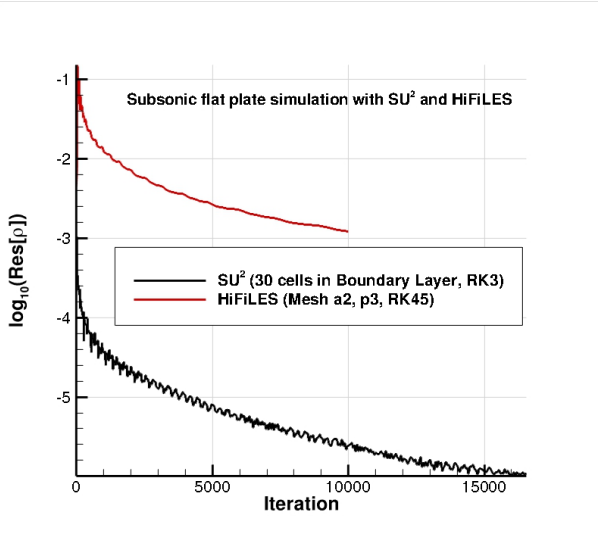

Figure 10: Comparison of HiFiLES with SU^2 using a similar time integration scheme.

To finalize, it is critical to note that the absence of a local time stepping technique in HiFiLES increases the required number of iterations to obtain a converged solution. However, we have noticed an improvement of the rate of convergence as we refine the grid (see Fig. 9). The obtained convergence rate is comparable to a second order numerical code (e.g. SU^2 [31,32]) running using a similar numerical time integration (see Fig.10).

C. Circular Cylinder

The classic test case of laminar flow past a circular cylinder at low Reynolds number has also been chosen as a verification and validation case for the 2D Navier-Stokes equations in HiFiLES, and the results are compared to existing experimental data and simulation results[33]. Two separate cases are computed: first, the steady flow past the cylinder at $Re = 20$, and second, the unsteady flow past the cylinder at $Re = 100$, where the Reynolds number is based upon the diameter of the cylinder. For both cases, the Mach number is set to 0.1 in order to recover nearly incompressible flow for comparisons with the existing incompressible results. The remaining flow conditions are 0° angle of attack, a constant ratio of specific heats of 1.4, a Prandtl number of 0.72, a free-stream temperature of 300 K, and a free-stream dynamic viscosity of $1.853 \cdot 10^{-5} Pa \cdot s$ (laminar viscosity varies according to Sutherland's law during the simulation).

The two simulations are performed with third order polynomials on a mesh with 4988 total elements that contains quadrilateral elements near the body of the cylinder and triangular elements out to the far-field. There is a small refinement box immediately downstream of the cylinder to help resolve features in the wake. The rectangular far-field boundaries are located approximately 30 diameters away from the cylinder in the upstream, upward, and downward directions and 50 diameters away in the downstream direction. A view of the mesh near the cylinder surface is shown in Fig. 11.

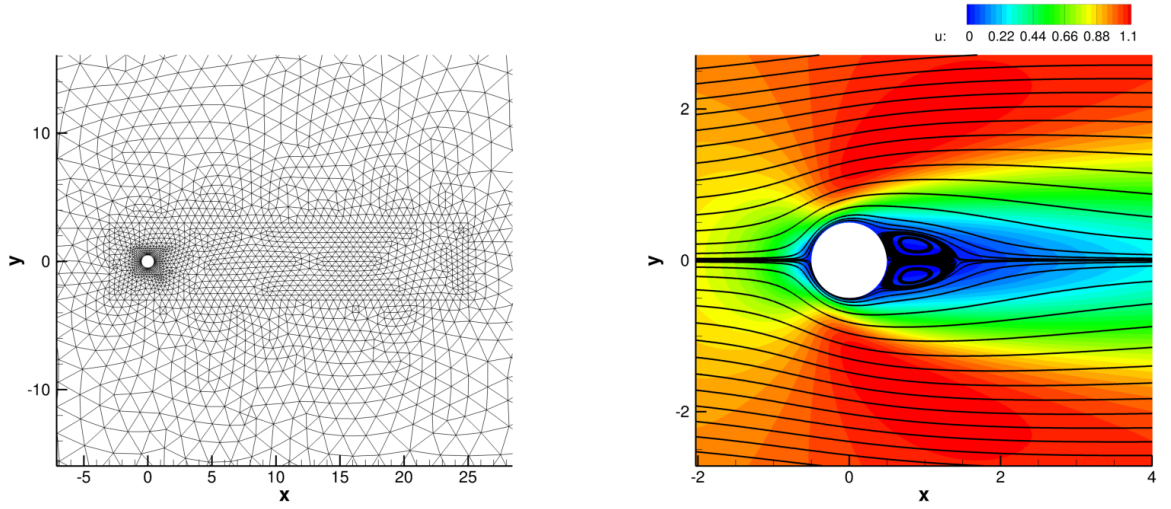

(a) Zoom view of the mesh near the cylinder.

(b) X-velocity contours and streamlines around the circular cylinder for $Re = 20$.

Figure 11: The mesh for the circular cylinder simulations along with x-velocity contours for the $Re = 20$ case.

The flow around the cylinder for $Re = 20$ is steady, and it features a large recirculation region behind the cylinder. Fig. 11 presents x-velocity contours around the cylinder along with streamlines. The length of the recirculation region can be determined from the streamlines, and a length of approximately one cylinder diameter agrees well with reported results for $Re = 20$. The coefficient of drag computed by HiFiLES is 2.043, which is close to the value of 2.01 reported by Park et al. Pressure contours around the cylinder are shown in Fig. 12.

When the Reynolds number is increased to 100, the flow around the cylinder becomes unsteady and exhibits periodic vortex shedding. This periodic shedding in the wake behind the cylinder can be seen in the instantaneous contours of x-velocity and vorticity in Fig. 13, and it also results in periodic fluctuations in the force coefficients on the cylinder. HiFiLES reports an average drag coefficient of 1.339 with a maximum deviation from this value of 0.0092, which agree excellently with the values reported by Park et al. of 1.33 and 0.0091 for the average C_d and maximum deviation from it, respectively. Instantaneous pressure contours for the $Re = 100$ case can be seen in Fig. 12. The asymmetry that is visible in the pressure contours contributes to the variability in the drag coefficient.

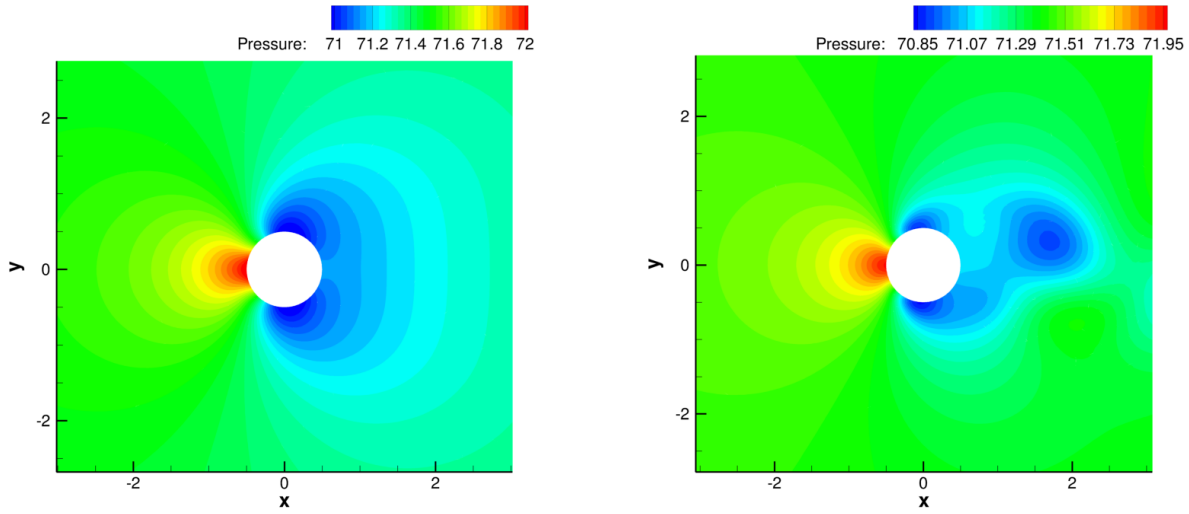

(a) Pressure contours for the $Re = 20$ case.

(b) Pressure contours for the $Re = 100$ case.

Figure 12: Pressure contours for the steady and unsteady (instantaneous) cylinder cases.

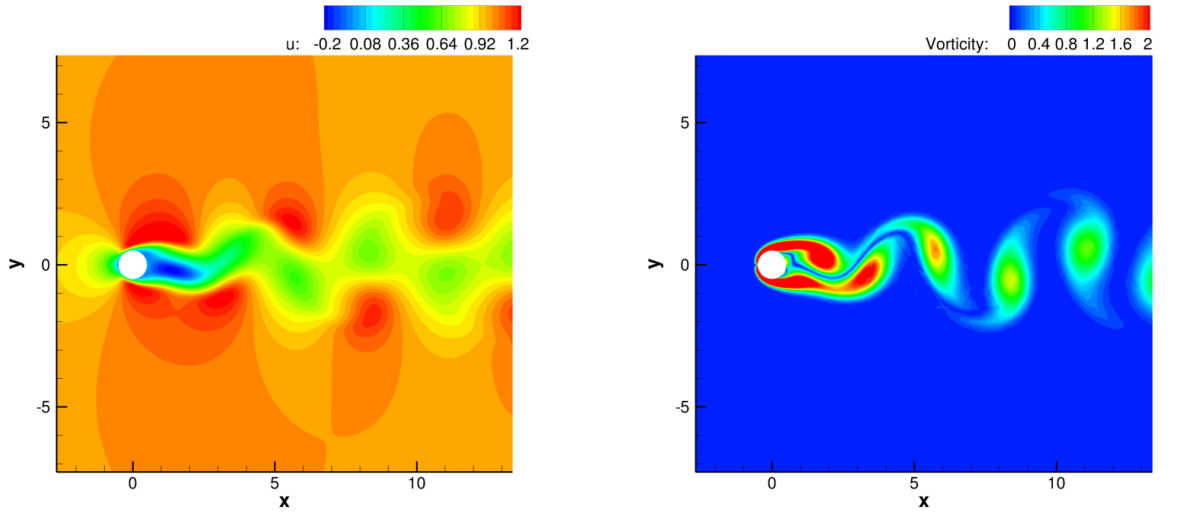

(a) X-velocity contours around the circular cylinder for $Re = 100$.

(b) Vorticity contours for the $Re = 100$ case.

Figure 13: Instantaneous solution contours for the unsteady cylinder case.

D. SD7003 airfoil at 4° angle of attack

Abundant literature documents flow around a SD7003 infinite wing and airfoil. Hence, physical experiments[34,35] and numerical simulations[36–40] of flow over this geometry can be used to benchmark HiFiLES.

The simulations on the 2D geometry were performed on a circular domain with a radius of $50c$, where c is the airfoil's cord length, centered at the leading edge of the airfoil. The boundary conditions are characteristic on the outer edge and adiabatic no-slip wall on the airfoil. The Mach number for all simulations was $M = 0.2$. The reported lift and drag coefficients in Table (6) correspond to the average of lift and drag coefficients over 13 periods after the flow reached a pseudo-periodic state. More details and figures of the detailed meshes are provided by Williams[41]. The total number of elements in the simulation was $N = 25,810$.

	$Re = 10K$		$Re = 22K$		$Re = 60K$	
Source	C_L	C_D	C_L	C_D	C_L	C_D
Uranga et al.[40]	0.3755	0.04978	0.6707	0.04510	0.5730	0.02097
c_{dg}, κ_{dg}	0.3719	0.04940	0.6722	0.04295	0.5831	0.01975
c_+, κ_+	0.3713	0.04935	0.6655	0.04275	0.5774	0.02005

Table 6: Time-averaged values of the lift and drag coefficients for the SD7003 airfoil flows with $Re = 10,000, 22,000, 60,000$. For information on the schemes labeled c_{dg}, κ_{dg}, and c_+, κ_+, the reader is referred to Williams's thesis[41]

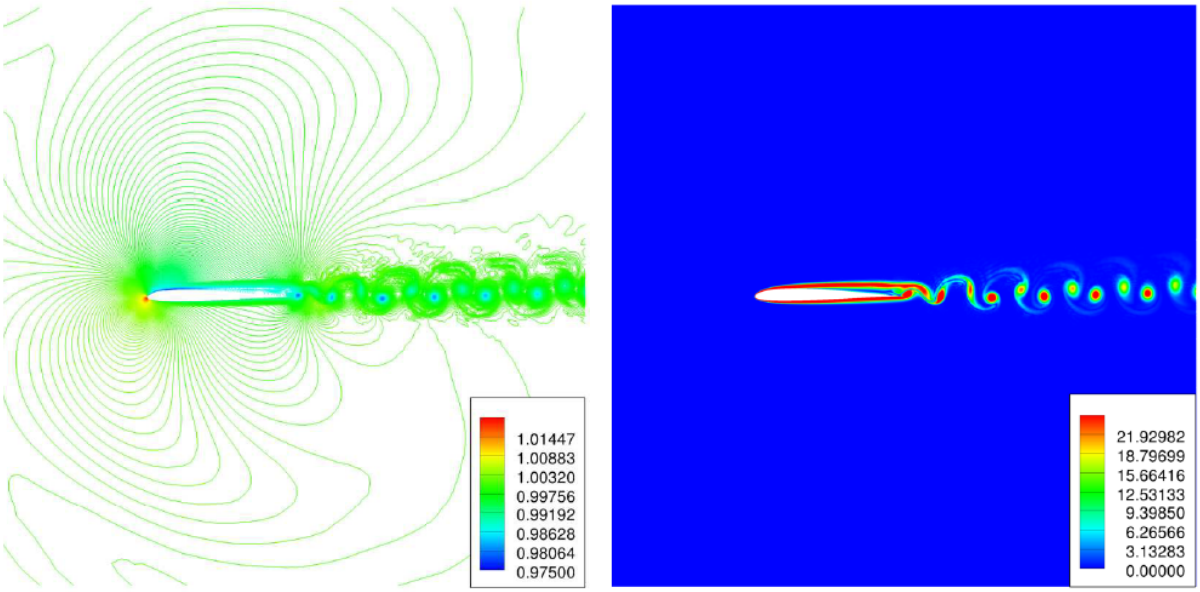

(a) Density contours

(b) Vorticity contours

Figure 14: Density and vorticity contours for the flow with $Re = 10,000$ around the SD7003 airfoil. The results were obtained using a polynomial basis with $p = 2$ on an unstructured triangular grid with $N = 25,810$ elements

The average lift and drag coefficients are in close agreement with the results by Uranga el. al[40]. The density contours in Figures (14),(15), and (16) show that vortical structures are captured for a reasonable distance away from the airfoil despite the fact that elements are coarser away from the airfoil.

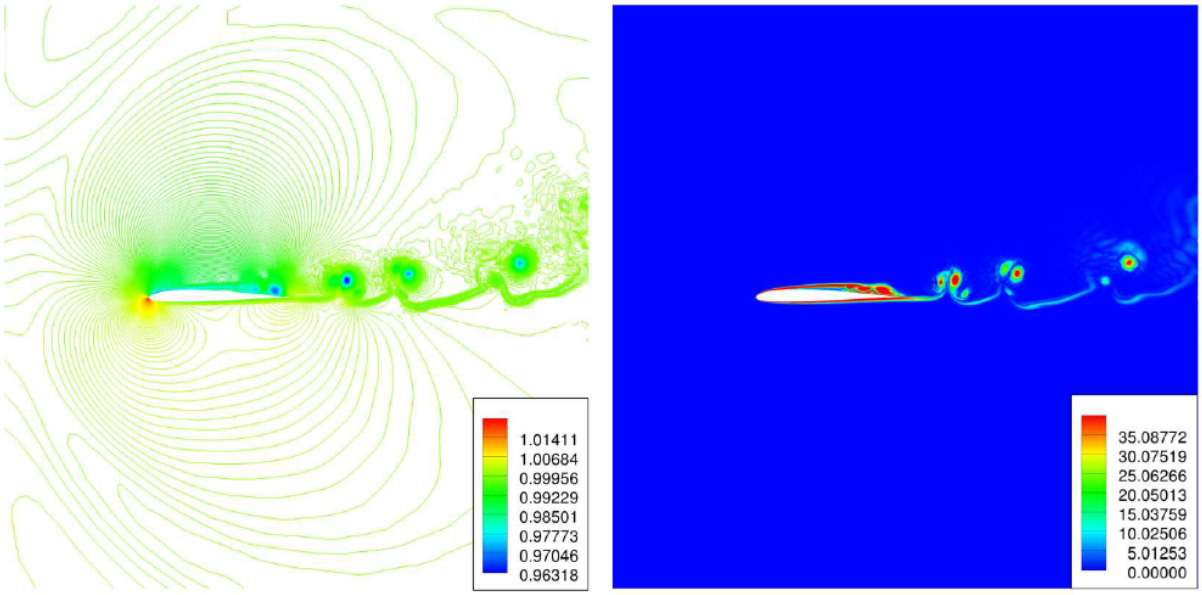

(a) Density contours (b) Vorticity contours

Figure 15: Density and vorticity contours for the flow with $Re = 22,000$ around the SD7003 airfoil. The results were obtained using a polynomial basis with $p = 2$ on an unstructured triangular grid with $N = 25,810$ elements

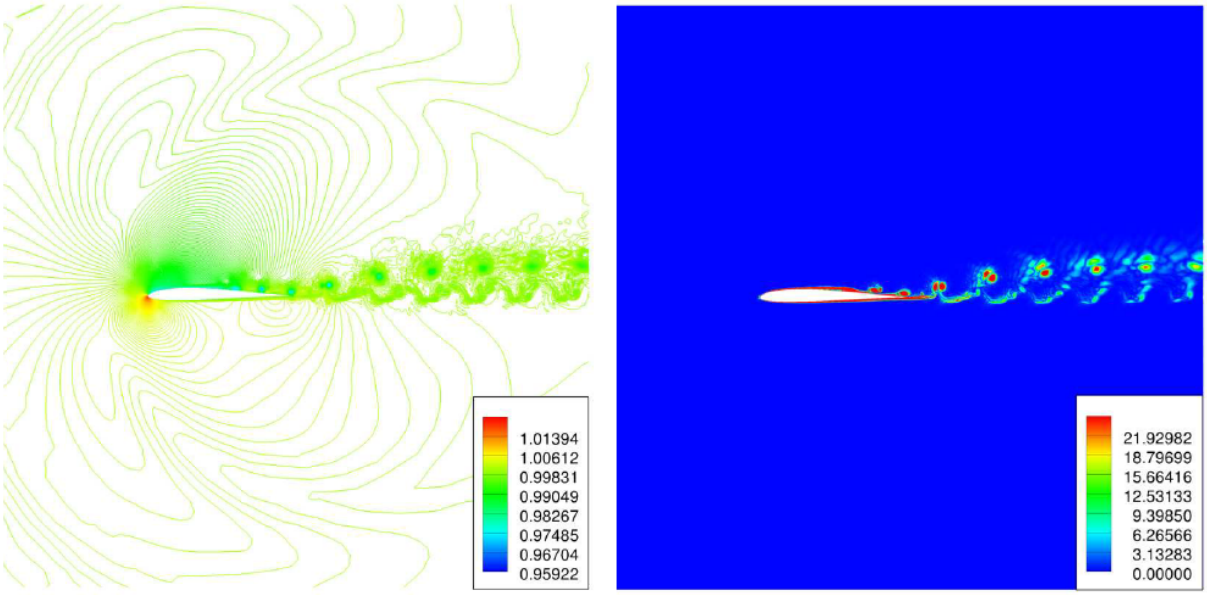

(a) Density contours (b) Vorticity contours

Figure 16: Density and vorticity contours for the flow with $Re = 60,000$ around the SD7003 airfoil. The results were obtained using a polynomial basis with $p = 2$ on an unstructured triangular grid with $N = 25,810$ elements

E. SD7003 wing section at 4° angle of attack

To validate HiFiLES's performance in 3D simulations, we extrude the SD7003 geometry from Section(D.) by $0.2c$ in the z-direction and apply periodic boundary conditions at $z = 0$ and $z = 0.2c$. Table (7) shows the time-averaged lift and drag coefficients. The total number of tetrahedral elements is $N = 711,332$.

	$Re = 10K$	
Source	C_L	C_D
Uranga et al.[40]	0.3743	0.04967
c_{dg}, κ_{dg}	0.3466	0.04908
c_+, κ_+	0.3454	0.04903

Table 7: Time-averaged values of the lift and drag coefficients for the SD7003 wing-section in a flow with $Re = 10,000$

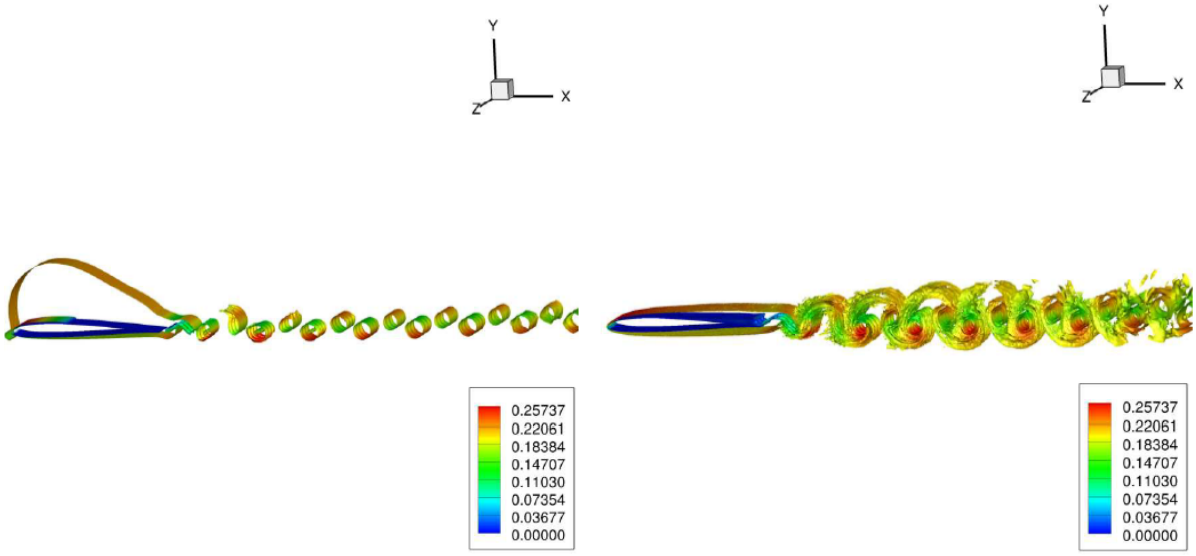

(a) Density contours

(b) Vorticity contours

Figure 17: Density and vorticity isosurfaces colored by Mach number for the flow with $Re = 10,000$ around the SD7003 wing-section. The results were obtained using a polynomial basis with order $p = 3$ on an unstructured tetrahedral grid with $N = 711,332$ elements.

F. Taylor-Green Vortex at Re = 1,600

The Taylor-Green Vortex (TGV) is a simple test of the resolution of the small scales of a turbulent flow by a numerical method. The compressible TGV at $Re = 1600$ was one of the benchmark problems in the 1st and 2nd International Workshops on High-Order CFD Methods[42]. A reference solution was computed by Debonis[43] using a high-order dispersion relation-preserving (DRP) scheme on a mesh of 512^3 elements. The results presented here were obtained by Bull and Jameson using FR to recover the fourth-order-accurate DG and SD schemes in HiFiLES[27,44]. We also compare our results to those of Beck and Gassner[45], who used a fourth-order filtered DG method on a mesh of 64^3 elements. From a simple initial condition in a triply-periodic box of dimensions $[0 : 2\pi]^3$, interactions between vortices cause the flow to develop in a prescribed manner into a mass of elongated vortices across a range of scales. The initial condition is specified as

$$u(t_0) = u_0 \sin(x/L)\cos(y/L)\cos(z/L), \tag{45}$$

$$v(t_0) = -u_0 \cos(x/L)\sin(y/L)\cos(z/L), \tag{46}$$

$$w(t_0) = 0, \tag{47}$$

$$p(t_0) = p_0 + \frac{\rho_0 V_0^2}{16}\left[\cos\left(\frac{2x}{L}\right) + \cos\left(\frac{2y}{L}\right)\right]\left[\cos\left(\frac{2z}{L}\right) + 2\right], \tag{48}$$

where $L = 1$, $u_0 = 1$, $\rho_0 = 1$ and $p_0 = 100$. The Mach number is set to 0.08 (consistent with the initial pressure p_0) and the initial temperature is 300K.

Figs. 18 (a) and (b) show the volume-averaged kinetic energy $\langle k \rangle$ on (a) hexahedral meshes of 16^3, 32^3 and 64^3 elements and (b) tetrahedral meshes (formed by splitting the hexahedral meshes in six). The reference solution, labelled as'DRP-512' is plotted for comparison. Figs. 18 (c) and (d) show the kinetic energy dissipation rate, given by $\epsilon = -d\langle k \rangle/dt$ versus the reference solution and the results of Beck and Gassner[45], labelled as'Beck-DG-64x4'. On the finest hexahedral and tetrahedral meshes the kinetic energy and dissipation rate predictions match the reference solution, demonstrating that the high-order numerical scheme is able to resolve the important flow dynamics on a relatively coarse mesh. As a qualitative measure of the resolution of the turbulent flow structures, Figure 19 shows isosurfaces of the q criterion at four times during the simulation. The evolution of complex small scale structures is evident.

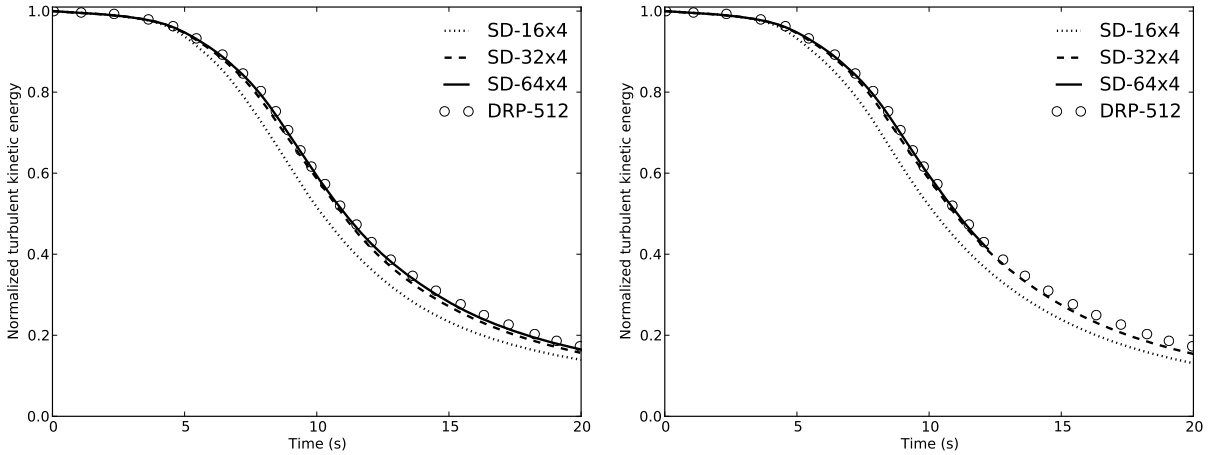

(a) $\langle k \rangle$, hexahedral meshes

(b) $\langle k \rangle$, tetrahedral meshes

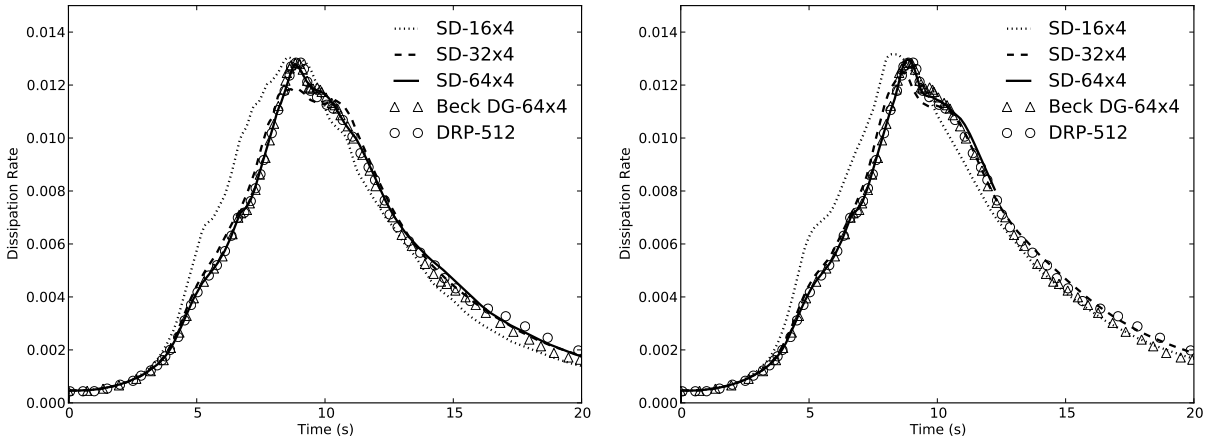

(c) $-d\langle k \rangle / dt$, hexahedral meshes

(d) $-d\langle k \rangle / dt$, tetrahedral meshes

Figure 18: Taylor-Green vortex results on hexahedral and tetrahedral meshes from Bull and Jameson[27]. (a, b) Evolution of average kinetic energy $\langle k \rangle$; (c, d) dissipation rate $-d\langle k \rangle / dt$. 'SD-$M \times N$' refers to M^3 mesh, Nth-order accurate SD scheme. (**- -**) 4th-order DG on 64^3 mesh[45]; (○) DNS[43].

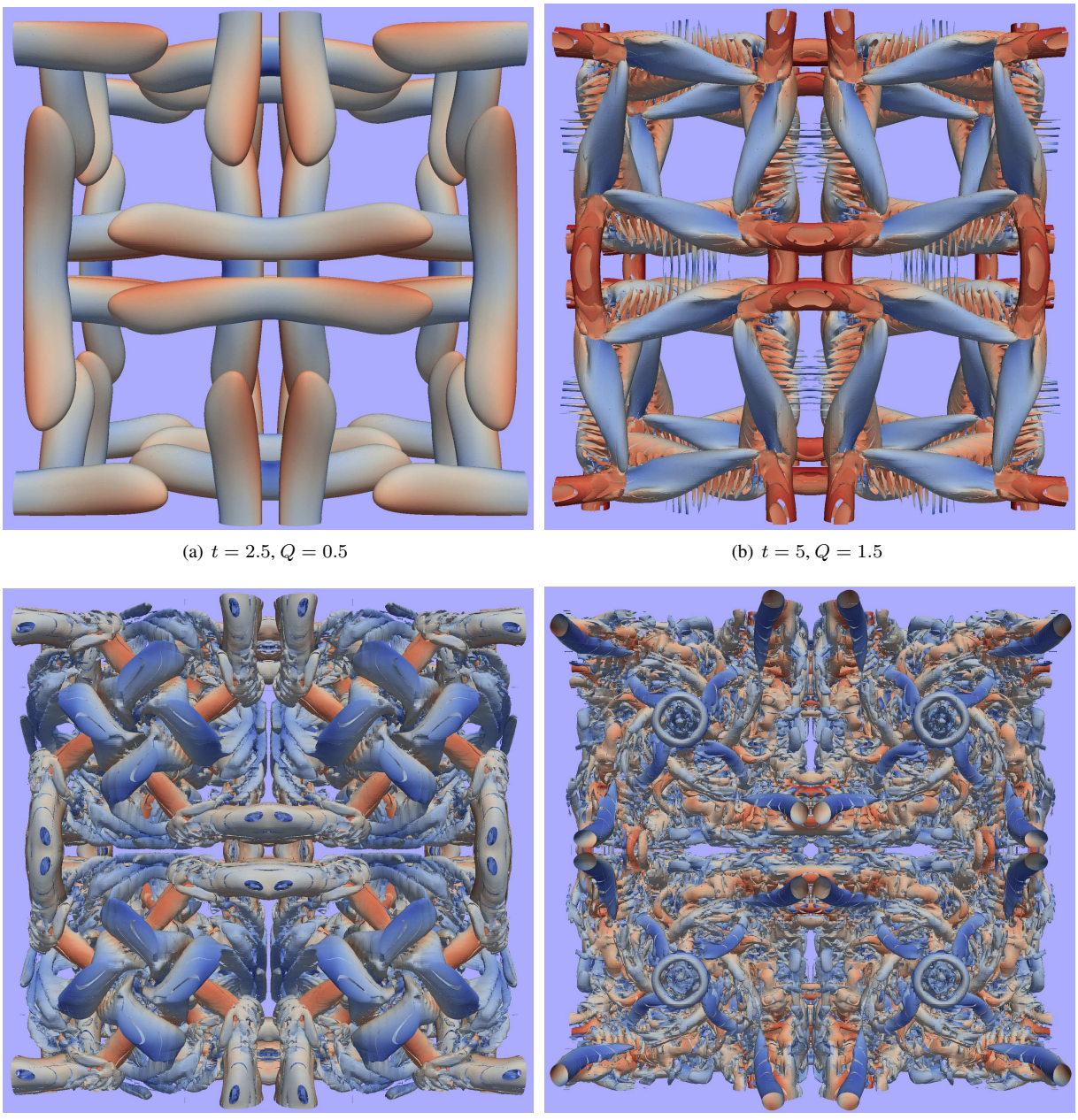

(a) $t = 2.5, Q = 0.5$

(b) $t = 5, Q = 1.5$

(c) $t = 7.5, Q = 1.5$

(d) $t = 10.75, Q = 1.5$

Figure 19: TGV solution on the fine mesh using fourth order accurate DG method, showing isosurfaces of q criterion colored by velocity magnitude at time t = 2.5 to 10.75 seconds.

G. LES of Flow Over a Square Cylinder at Re = 21,400

Using the FR method to recover the fourth-order accurate SD scheme, the flow over a square cylinder of side D in a domain of $21D \times 12D \times 3.2D$ (see Figure 20) at $Re = 21,400$ and Mach 0.3 was simulated, for which Laser Doppler Velocimetry (LDV) experimental data is available[46,47]. A tetrahedral mesh of 87,178 elements was generated giving a total of 1.74M degrees of freedom (D0F) since there are 20 solution points per element at fourth order accuracy. Time discretization was by the fourth-order five-stage explicit RK scheme. A total time of 250 seconds was simulated and time-averaged quantities were calculated over the last 100 seconds (approx. 5 flow-through periods). The WSM model (see Section E.) based on the modal Vandermonde filter[27] was used with the Breuer-Rodi three-layer wall model[48] within 0.2D of the wall. The computation took around 60 hours on 7 GPUs in the lab's own cluster. Figure 20 shows the computational mesh including all the DoFs. Figure 21 shows an isosurface of the q-criterion colored by velocity magnitude, illustrating the structures present in the turbulent boundary layer and wake. Figures 22 (a, b) show the normalized mean streamwise and vertical velocity components $\langle u \rangle / u_B$ and $\langle v \rangle / u_B$ respectively along several vertical lines in the wake. Figures 22 (c, d) show the normalized mean Reynolds stress components $\langle u'u' \rangle / u_B^2$ and $\langle u'v' \rangle / u_B^2$ along the same lines. For comparison, high-order LES results computed by Lodato and Jameson[23] using the SD method and the WSM model on a hexahedral mesh of 2.3M DoF are plotted. Mean velocities are accurately predicted although the accuracy is reduced near the cylinder owing to the coarse tetrahedral resolution in the boundary layer. The Reynolds stresses are less accurately predicted than the mean velocities but are broadly correct. These results highlight the advantages of using HiFiLES for LES of turbulent flows: the ability to obtain good results on coarse meshes and the ability to use unstructured tetrahedral meshes.

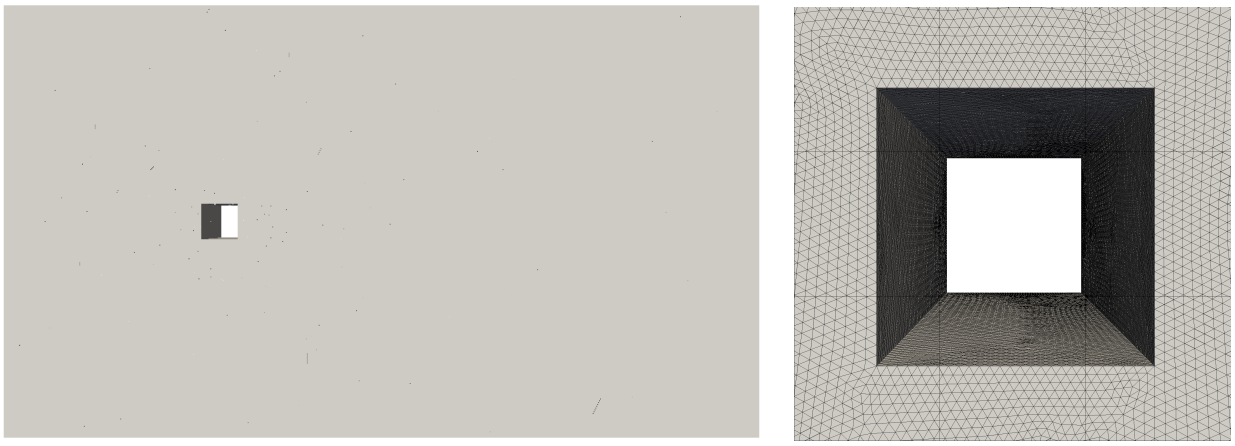

(a) geometry (b) boundary layer mesh

Figure 20: Square cylinder geometry and tetrahedral boundary layer mesh showing all degrees of freedom

Figure 21: Isosurface of the q-criterion colored by velocity magnitude showing the wake behind the square cylinder

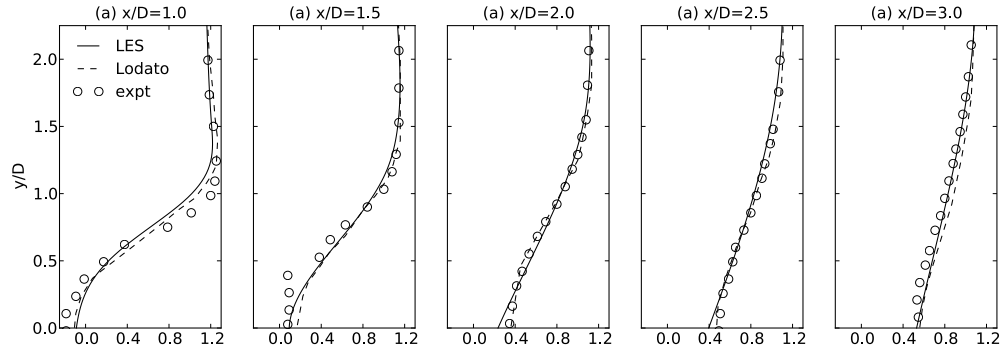

(a) Mean streamwise velocity $\langle u \rangle / u_B$

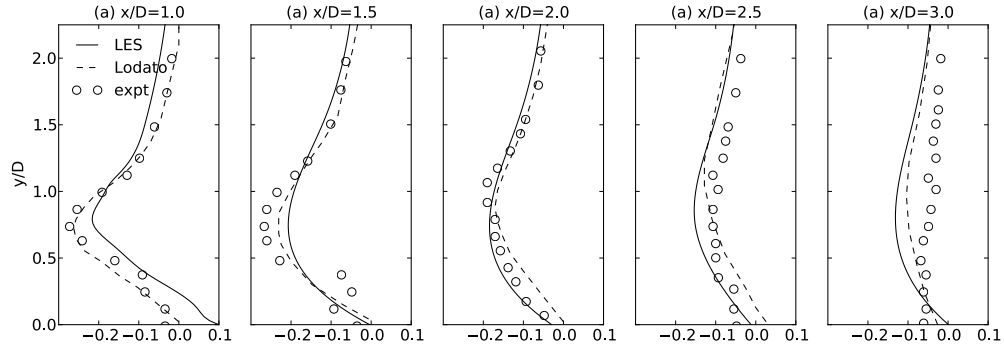

(b) Mean vertical velocity $\langle v \rangle / u_B$

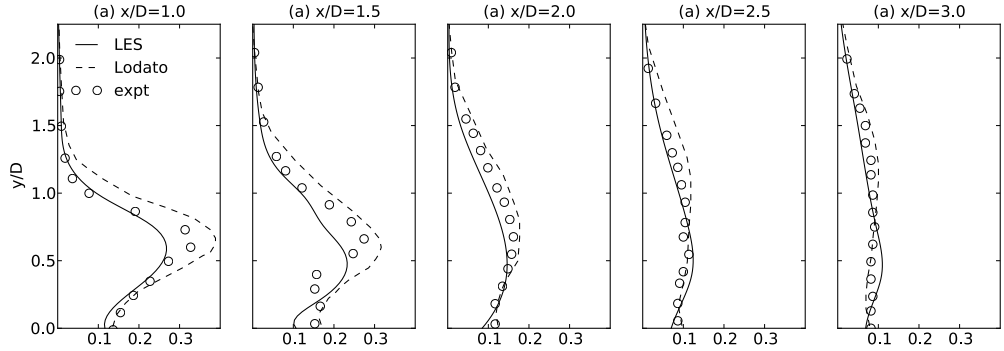

(c) Mean Reynolds stress $\langle u'u' \rangle / u_B^2$

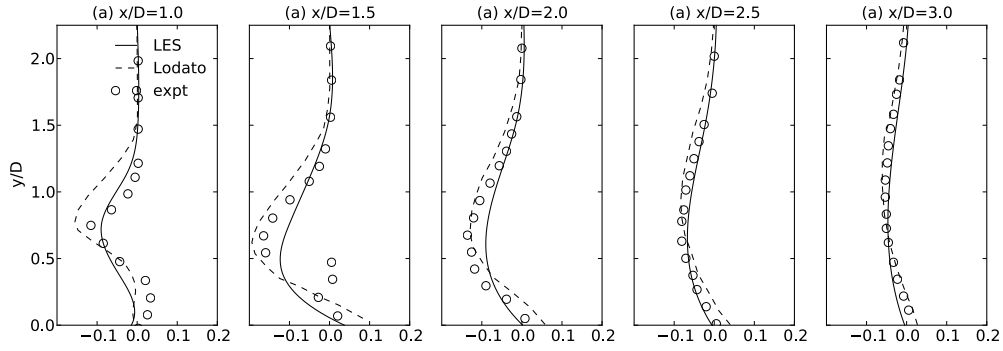

(d) Mean Reynolds stress $\langle u'v' \rangle / u_B^2$

Figure 22: (a) Mean streamwise and vertical velocity and mean Reynolds stresses along vertical lines in the wake. (—) current results, (- - -) 4th order SD+WSM on hexahedral mesh by Lodato and Jameson[23], (○) LDV experiments by Lyn et al.[46,47].

H. NACA 0012 airfoil at 0° angle of attack, Re = 6 million, M = 0.15

In this section, the NACA 0012 airfoil is used to study the accuracy of the SA turbulence model coupled with FR. The NACA 0012 is commonly used as a validation case for all turbulence models and a large database of results are available at the NASA Turbulence Modeling Resource website. A 6,539 element quad/triangle mixed mesh is used with a NACA 0012 airfoil of chord length 1.0 and a farfield boundary 20 chord lengths away. The results are compared with CFL3D and experimental results from Gregory & O'Reilly, NASA R&M 3726, Jan 1970.

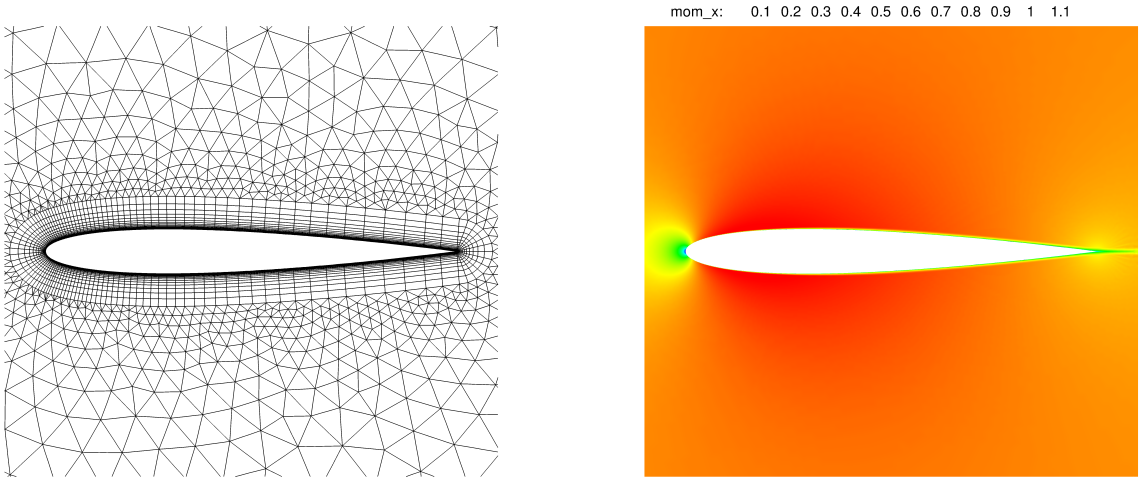

(a) Zoomed view of the mixed element mesh near the NACA 0012 airfoil.

(b) X-momentum contours near the NACA 0012 airfoil

Figure 23: Turbulent flow past a NACA 0012 airfoil at Re = 6 million, M = 0.15, $\alpha = 0°$ using FR to recover 4th order accurate DG method and the SA turbulence model.

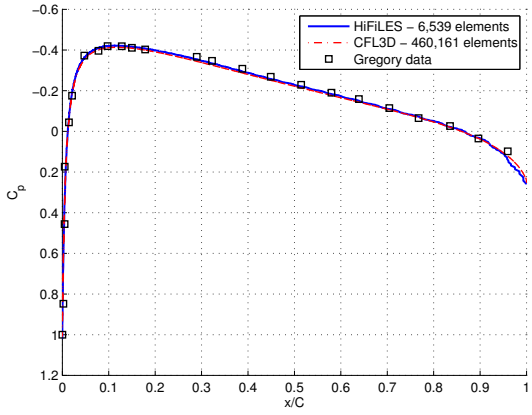

Figure 24: Pressure coefficient on the NACA 0012 airfoil at Re = 6 million, M = 0.15, $\alpha = 0°$ using FR to recover 4th order accurate DG method and the SA turbulence model.

V. Conclusion

In this work, we have presented a comprehensive description, verification and validation of the HiFiLES solver. In its first version, HiFiLES offers to its users an implementation of the Flux Reconstruction methodology on unstructured 3D grids optimized for using GPUs or traditional MPI. The implementation has been verified via the method of manufactured solutions. The code has been tested in some difficult Navier-Stokes and Large Eddy Simulation problems with very satisfactory results.

The power of the Flux Reconstruction method is in its flexibility, efficiency and accuracy. Different high-order schemes can be recovered by choosing a single parameter, allowing the numerical behavior to be fine-tuned. Despite its advantages, FR is not yet as popular as other high-order methods, but we hope that, thanks to this work, the benefits of the method will be communicated to a much wider audience. Though the use of explicit timestepping sets limits on the CFL condition, the fact that HiFiLES can be run on high performance multi-GPU platforms may compensate for this.

Despite considerable advances in the accuracy and versatility of subgrid-scale models, current industrial CFD codes are restricted in their ability to perform LES of turbulent flows by the use of highly dissipative second-order numerical schemes. Therefore, in order to advance the state of the art in industrial CFD, it is necessary to move to high-order accurate numerical methods. The ESFR family of schemes are ideal for resolving turbulent flows due to low numerical dissipation and high-order accurate representation of solution gradients at the small scales. Advanced subgrid-scale models have been implemented in HiFiLES for all element types, enabling simulation of turbulent flows over complex geometry. The development of the first open-source, high-order accurate solver for unstructured meshes incorporating LES modeling capabilities represents a significant step towards tackling challenging compressible turbulent flow problems of practical interest. Future work will include stabilization techniques, optimization of the ESFR schemes for turbulence resolution, moving mesh capabilities, local time-stepping, multigrid convergence acceleration and advanced turbulence modeling.

Acknowledgements

The authors would like to acknowledge the support for this work provided by the Stanford Graduate Fellowships, National Science Foundation Graduate Fellowships, the National Science Foundation under Grant 1114816, and the Air Force Office of Scientific Research under Grant FA9550–10–1–0418.

References

[1]Castonguay, P., Williams, D., Vincent, P., López-Morales, M. R., and Jameson, A., "On the Development of a High-Order, Multi-GPU Enabled, Compressible Viscous Flow Solver for Mixed Unstructured Grids," *AIAA Computational Fluid Dynamics Conference, AIAA-2011-3229*, 2011.

[2]Landau, L. and Lifshitz, E., *Fluid Mechanics (2nd Edition)*, Pergamon Press, 1993.

[3]Wilcox, D. C., *Turbulence modeling for CFD*, Vol. 2, DCW industries La Canada, CA, 1998.

[4]Oliver, T. A., Tech. rep., DTIC Document, 2008.

[5]Hesthaven, J. and Warburton, T., *Nodal discontinuous Galerkin methods: algorithms, analysis, and applications*, Vol. 54, Springer, 2007.

[6]Castonguay, P., Williams, D., Vincent, P., and Jameson, A., "Energy stable flux reconstruction schemes for advection–diffusion problems," *Computer Methods in Applied Mechanics and Engineering*, Vol. 267, 2013, pp. 400–417.

[7]Huynh, H., "A flux reconstruction approach to high-order schemes including discontinuous Galerkin methods," *AIAA paper*, Vol. 4079, 2007, pp. 2007.

[8]Vincent, P. E., Castonguay, P., and Jameson, A., "A new class of high-order energy stable flux reconstruction schemes," *Journal of Scientific Computing*, Vol. 47, No. 1, 2011, pp. 50–72.

[9]Huynh, H., "A flux reconstruction approach to high-order schemes including discontinuous Galerkin methods," *AIAA paper*, Vol. 4079, 2007, pp. 2007.

[10]Castonguay, P., Vincent, P. E., and Jameson, A., "A new class of high-order energy stable flux reconstruction schemes for triangular elements," *Journal of Scientific Computing*, Vol. 51, No. 1, 2012, pp. 224–256.

[11]Williams, D., Castonguay, P., Vincent, P. E., and Jameson, A., "Energy stable flux reconstruction schemes for advection–diffusion problems on triangles," *Journal of Computational Physics*, Vol. 250, 2013, pp. 53–76.

[12]Williams, D. and Jameson, A., "Energy Stable Flux Reconstruction Schemes for Advection–Diffusion Problems on Tetrahedra," *Journal of Scientific Computing*, 2013, pp. 1–39.

[13]Jameson, A., "Advances in bringing high-order methods to practical applications in computational fluid dynamics," *AIAA paper*, Vol. 3226, 2011.

[14]Sheshadri, A. and Jameson, A., "Shock detection and capturing methods in high order Discontinuous Galerkin Finite Element Methods," 2014.

[15]Persson, P. and Peraire, J., "Sub-Cell Shock Capturing for Discontinuous Galerkin Methods," Tech. rep., 2006.

[16]Persson, P., "Shock Capturing for High-Order Discontinuous Galerkin Simulation of Transient Flow Problems," 21st aiaa computational fluid dynamics conference proceedings 2013-3061, 2013.

[17]Spalart, P. and Allmaras, S., "A one-equation turbulence model for aerodynamic flows," 1992.

[18]Burgess, N. K. and Mavriplis, D. J., "Robust computation of turbulent flows using a discontinuous Galerkin method," *AIAA paper*, Vol. 457, 2012.

[19]Moro, D., Nguyen, N., and Peraire, J., "Navier-stokes solution using hybridizable discontinuous galerkin methods," *AIAA Paper*, Vol. 3407, 2011, pp. 2011.

[20]Smagorinsky, J., "General circulation experiments with the primitive equations," *Monthly Weather Review*, Vol. 91, No. 3, 1963, pp. 99–164.

[21]Nicoud, F. and Ducros, F., "Subgrid-Scale Stress Modelling Based on the Square of the Velocity Gradient Tensor," *Flow, Turbulence and Combustion*, Vol. 62, No. 3, September 1999, pp. 183–200.

[22]Bardina, J., Ferziger, J., and Reynolds, W., "Improved subgrid-scale models for large-eddy simulation," *13th AIAA Fluid and Plasma Dynamics Conference*, Snowmass, Colo., July 14-16, 1980, July 1980.

[23]Lodato, G., Castonguay, P., and Jameson, A., "Discrete filter operators for large-eddy simulation using high-order spectral difference methods," *Int. J. Numer. Meth. Fl.*, Vol. in press, 2012.

[24]Vasilyev, O. V., Lund, T. S., and Moin, P., "A General Class of Commutative Filters for LES in Complex Geometries," *Journal of Computational Physics*, Vol. 146, 1998, pp. 82–104.

[25]Vasilyev, O. V., Marsden, A. L., and Moin, P., "Construction of Commutative Filters for LES on Unstructured Meshes," *Journal of Computational Physics*, Vol. 175, 2002, pp. 584–603.

[26]Blackburn, H. and Schmidt, S., "Spectral element filtering techniques for large eddy simulation with dynamic estimation," *Journal of Computational Physics*, Vol. 186, 2003, pp. 610–629.

[27]Bull, J. and Jameson, A., "High-Order Flux Reconstruction Schemes for LES on Tetrahedral Meshes," *Notes on Numerical Fluid Mechanics and Multidisciplinary Design, Vol.*, edited by W. Haasse, Springer, May 2014, unpublished.

[28]Lodato, G., Vervisch, L., and Domingo, P., "A Compressible Wall-Adapting Similarity Mixed Model for Large-Eddy Simulation of the Impinging Round Jet," *Physics of Fluids*, Vol. 21, No. 3, 2009.

[29]Salari, K. and Knupp, P., "Code verification by the method of manufactured solutions," Tech. rep., Sandia National Labs., Albuquerque, NM (US); Sandia National Labs., Livermore, CA (US), 2000.

[30]Carpenter, M. H. and Kennedy, C. A., "Fourth-order 2N-storage Runge-Kutta schemes," *Nasa tm*, Vol. 109112, 1994.

[31]Palacios, F., Colonno, M., C.Aranake, A., Campos, A., Copeland, S. R., Economon, T. D., Lonkar, A. K., Lukaczyk, T. W., Taylor, T. W. R., and Alonso, J. J., "Stanford University Unstructured (SU2): An open-source integrated computational environment for multi-physics simulation and design," *51st AIAA Aerospace Sciences Meeting including the New Horizons Forum and Aerospace Exposition*, AIAA Paper 2013-0287, Grapevine, Texas, January 2013.

[32]Palacios, F., Economon, T. D., Aranake, A. C., Copeland, S. R., Lonkar, A. K., Lukaczyk, T. W., Manosalvas, D. E., Naik, K. R., Padron, A. S., Tracey, B., Variyar, A., and Alonso, J. J., "Stanford University Unstructured (SU^2): Open-source analysis and design technology for turbulent flow," *52nd AIAA Aerospace Sciences Meeting*, AIAA Paper 2014-0243, National Harbor, Maryland, January 2014.

[33]Park, J., Kwon, K., and Choi, H., "Numerical solutions of flow past a circular cylinder at Reynolds numbers up to 160," *KSME International Journal*, Vol. 12, No. 6, 1998, pp. 1200–1205.

[34]Ol, M. V., McAuliffe, B. R., Hanff, E. S., Scholz, U., and Kähler, C., "Comparison of laminar separation bubble measurements on a low Reynolds number airfoil in three facilities," *AIAA paper*, Vol. 5149, No. 1, 2005, pp. 2005.

[35]Radespiel, R. E., Windte, J., and Scholz, U., "Numerical and experimental flow analysis of moving airfoils with laminar separation bubbles," *AIAA journal*, Vol. 45, No. 6, 2007, pp. 1346–1356.

[36]Galbraith, M. and Visbal, M., "Implicit large eddy simulation of low Reynolds number flow past the SD7003 airfoil," *AIAA paper*, Vol. 225, 2008, pp. 2008.

[37]Visbal, M. R., Gordnier, R. E., and Galbraith, M. C., "High-fidelity simulations of moving and flexible airfoils at low Reynolds numbers," *Experiments in Fluids*, Vol. 46, No. 5, 2009, pp. 903–922.

[38]Castonguay, P., Liang, C., and Jameson, A., "Simulation of transitional flow over airfoils using the spectral difference method," *AIAA paper*, Vol. 4626, 2010, pp. 2010.

[39]Persson, P.-O., "High-Order LES Simulations using Implicit-Explicit Runge-Kutta Schemes," 2010.

[40]Uranga, A., Persson, P.-O., Drela, M., and Peraire, J., "Implicit Large Eddy Simulation of transition to turbulence at low Reynolds numbers using a Discontinuous Galerkin method," *International Journal for Numerical Methods in Engineering*, Vol. 87, No. 1-5, 2011, pp. 232–261.

[41]Williams, D. M., *Energy Stable High-Order Methods for Simulating Unsteady, Viscous, Compressible Flows on Unstructured Grids*, Ph.D. thesis, Stanford University, 2013.

[42]Wang, Z., Fidkowski, K., Abgrall, R., Bassi, F., Caraeni, D., Cary, A., Deconinck, H., Hartmann, R., Hillewaert, K., Huynh, H., Kroll, N., May, G., Persson, P.-O., van Leer, B., and Visbal, M., "High-Order CFD Methods: Current Status and Perspective High-Order CFD Methods: Current Status and Perspective," *International Journal for Numerical Methods in Fluids*, Vol. 72, No. 8, 2013, pp. 811–845.

[43]Debonis, J., "Solutions of the Taylor-Green Vortex Problem Using High-Resolution Explicit Finite Difference Methods," *AIAA Paper 2013-0382*, 2013.

[44]Bull, J. and Jameson, A., "Simulation of the Compressible Taylor Green Vortex using High-Order Flux Reconstruction Schemes," *AIAA Aviation 2014, 16–20 June, Atlanta, Georgia*, June 2014, unpublished.

[45]Beck, A. and Gassner, G., "On the accuracy of high-order discretizations for underresolved turbulence simulations," *Theoretical and Computational Fluid Dynamics*, Vol. 27, No. 3-4, 2012, pp. 221–237.

[46]Lyn, D. and Rodi, W., "The flapping shear layer formed by flow separation from the forward corner of a square cylinder," *J. Fluid Mech.*, Vol. 267, 1994, pp. 353–376.

[47]Lyn, D., Einav, S., Rodi, W., and Park, J., "A laser-Doppler velocimetry study of ensemble-averaged characteristics of the turbulent near wake of a square cylinder," *J. Fluid Mech.*, Vol. 304, No. 1, 1995, pp. 285–319.

[48]Breuer, M. and Rodi, W., "Large-eddy simulation of turbulent flow through a straight square duct and a 180 bend," *Direct and Large-Eddy Simulation I*, Springer, 1994, pp. 273–285.